Depositing >1.5 Mt of Tin Within

Matthieu Harlaux, Daniel Kontak, Alan Clark, Kalin Kouzmanov, Christopher Holm-Denoma, Stefano Gialli, Oscar Laurent, Richard Spikings, Alain Chauvet, Andrea Dini, et al.

Depositing over 1.5 Mt of Sn within <1 Myr of initial granitic intrusion in the San Rafael Sn (-Cu) deposit, southeastern Peru

Matthieu Harlaux,[1,†,*] Daniel J. Kontak,[2] Alan H. Clark,[3] Kalin Kouzmanov,[4] Christopher S. Holm-Denoma,[5] Stefano Gialli,[4] Oscar Laurent,[6,††] Richard Spikings,[4] Alain Chauvet,[7] Andrea Dini,[8] Miroslav Kalinaj,[9] and Lluís Fontboté[4]

[1] Nevada Bureau of Mines and Geology, University of Nevada, Reno, Nevada 89557-0178, USA

[2] Harquail School of Earth Sciences, Sudbury, Ontario P3E 2C6, Canada

[3] Department of Geological Sciences and Geological Engineering, Queen's University, Kingston, Ontario K7L 3N6, Canada

[4] Department of Earth Sciences, University of Geneva, 1205 Geneva, Switzerland

[5] U.S. Geological Survey, Denver Federal Center, Denver, Colorado 80225-0046, USA

[6] Institute of Geochemistry and Petrology, ETH Zürich, 8092 Zürich, Switzerland

[7] Géosciences Montpellier, CNRS-UMR 5243, Université de Montpellier, 34095 Montpellier, France

[8] Istituto di Geoscienze e Georisorse, Consiglio Nazionale delle Ricerche (CNR), 56124 Pisa, Italy

[9] Minsur S.A., Jr. Lorenzo Bernini 149, San Borja, Lima 27, Peru

[†] Present address: BRGM – French Geological Survey, 45060 Orléans, France

[††] Present address: Géosciences Environnement Toulouse, CNRS-UMR 5563, Observatoire Midi-Pyrénées, Université Toulouse III Paul Sabatier, 31400 Toulouse, France

* Corresponding author: m.harlaux@brgm.fr

Abstract

The San Rafael Sn (-Cu) deposit, located in the Eastern Cordillera of southeast Peru, is one of the world's largest cassiterite-bearing vein systems (>1 Mt Sn produced since 1969). The deposit consists of a quartz-cassiterite-chlorite-sulfide lode system spatially associated with an upper Oligocene (ca. 24 Ma) S-type granitic pluton. Based on a revised paragenetic sequence for the deposit, we interpret the temporal setting of both magmatic (biotite, K-feldspar) and hydrothermal (muscovite, adularia, cassiterite) minerals analyzed by $^{40}Ar/^{39}Ar$ step-heating and U-Pb LA-ICP-MS geochronology. The least disturbed biotite sample from the megacrystic monzogranite yielded a $^{40}Ar/^{39}Ar$ plateau age of 24.10 ± 0.26 Ma (2σ), which constrains the time of cooling of the upper part of the pluton to below 300°C. Greisen developed on top of the granitic cupola and its immediate metamorphic aureole dated at 24.24 ± 0.24 Ma (2σ; $^{40}Ar/^{39}Ar$ muscovite average plateau age) is interpreted to be contemporaneous with the emplacement of pre-ore quartz-tourmaline veins and breccias. In situ U-Pb dating of cassiterite, including both botryoidal cassiterite ("wood tin") and coarse-grained cassiterite in quartz-chlorite veins and breccias, constrains the timing of the main Sn ore stage to between 24.10 ± 0.37 Ma and 23.47 ± 0.53 Ma (2σ). Botryoidal and coarse-grained cassiterite are characterized by similar trace element compositions with fluctuating metal concentrations across growth banding, suggesting significant changes of physicochemical conditions of the hydrothermal system during cassiterite precipitation, likely caused by rapid and repeated mixing between magmatic fluids and meteoric groundwaters. Polymetallic sulfide-rich veins and quartz-carbonate veins are constrained to have formed between 22.72 ± 0.11 Ma and 22.29 ± 0.24 Ma (2σ) based on adularia $^{40}Ar/^{39}Ar$ plateau ages. The latter overlap partially reset $^{40}Ar/^{39}Ar$ age spectra for K-feldspar megacrysts in the host granite and thus reflect pervasive alteration by hydrothermal fluids. Collectively the results show the magmatic-hydrothermal system spanned at least 2 Myr

with the main Sn ore stage representing <1 Myr in the lifetime of the deposit. The latest polymetallic stages postdate the main Sn ore stage by ca. 1 Myr and reflect the waning of the hydrothermal system accompanied by additional incursion of meteoric groundwaters. This study provides further evidence that the present-day exposed level of the San Rafael granite was a passive host for the Sn mineralization and only provided the structural focusing for the mineralizing fluids derived from a deeper part of the magmatic system.

Introduction

Determining the lifetime of magmatic-hydrothermal systems is of great importance as it provides the temporal constraints, or geological timescales, necessary for understanding processes responsible for the formation of ore deposits. In the last years, significant advances have been done to determine the duration of magmatic-hydrothermal processes, with a specific focus on the formation of porphyry Cu (-Au-Mo) systems, based on high-precision geochronology techniques (e.g., Deckart et al., 2005; Catchpole et al., 2015; Chelle-Michou et al., 2015; Buret et al., 2016; Tapster et al., 2016; Li et al., 2017; Rottier et al., 2020) and element diffusion modeling (e.g., Mercer et al., 2015; Cernuschi et al., 2018). High-precision U-Pb dating of igneous zircons has revealed periods of <1 Myr between magma crystallization and extraction of ore-forming fluids, with timespans as short as a few 10,000s yr between individual fluid pulses (e.g., Deckart et al., 2005; von Quadt et al., 2011; Chiaradia et al., 2013; Spencer et al., 2015; Tapster et al., 2016; Large et al., 2021). Until recently the lifetime of granite-related Sn and/or W deposits had yet to be investigated in such detail compared to porphyry Cu (-Mo) systems. New insight has been provided for the timing and duration of Sn±W ore deposit formation via U-Pb dating of ore minerals such as cassiterite and wolframite (e.g., Zhang et al., 2017; Harlaux et al., 2018a; Moscati and Neymark, 2020; Tang et al., 2020; Denholm et al.,

2021; Gemmrich et al., 2021; Carr et al., 2021). Importantly, most of the latter studies focused on several mineralized districts whereas there are only a few reported detailed geochronological results that have bracketed the duration of magmatic-hydrothermal events in a single Sn±W deposit (Hu et al., 2012; Chen et al., 2019; Carr et al., 2020; Mohammadi et al., 2020; Tapster and Bright, 2020; Legros et al., 2020; Harlaux et al., 2021a).

This paper presents a detailed geochronological study of the San Rafael Sn (-Cu) deposit, one of the world's largest granite-related cassiterite-bearing lode systems, that is located in the Central Andean tin belt of southeast Peru. The geological setting and paragenetic evolution of the San Rafael lode system were first studied by Arenas (1980), Palma (1981), and Kontak (1985), and then investigated in detail by Kontak and Clark (2002) and Mlynarczyk et al. (2003). The regional and metallogenic settings of mineralization were documented by Kontak (1985), Clark et al. (1983, 1990), Kontak et al. (1990a,b), and Sandeman et al. (1997), while the geodynamic evolution was outlined by Sandeman et al. (1995) and Mlynarczyk and Williams-Jones (2005). Major contributions to the petrology and geochemistry of the granitic host rocks and the alteration and mineralization processes at San Rafael were brought by Kontak and Clark (2002), Mlynarczyk et al. (2003), Mlynarczyk (2005), Mlynarczyk and Williams-Jones (2006), Wagner et al. (2009), Corthay (2014), Prado Flores (2015), Gialli et al. (2019), Harlaux et al. (2020, 2021b, 2021c), and Cazorla Martínez (2022). Building on a revised paragenetic sequence for the San Rafael deposit, we present the results of $^{40}Ar/^{39}Ar$ and U-Pb chronometers for magmatic (biotite, K-feldspar) and hydrothermal (muscovite, adularia, cassiterite) minerals to constrain the lifetime of the magmatic-hydrothermal ore system. We demonstrate that the hydrothermal system related to the San Rafael granitic pluton was active for a protracted period lasting at least 2 Myr during the late Oligocene to early Miocene. We also show that the main Sn mineralizing event spanned <1 Myr shortly after the emplacement of a composite granitic stock and associated dikes. Finally, we analyzed the major and trace

element composition of cassiterite to investigate its potential as a tracer of geologic processes during Sn deposition at San Rafael.

Geological Background

The San Rafael Sn (-Cu) deposit (latitude 14°13’58” S, longitude 70°19’18” W) is located within the Cordillera de Carabaya in the Eastern Cordillera of southeast Peru (Fig. 1A). This segment belongs to the Central Andean tin belt which extends from southern Peru, through Bolivia, to northern Argentina and hosts hundreds of Sn-W±Ag-Cu deposits and occurrences located within a 1,000-km-long and 30- to 130-km-wide belt (Kelly and Turneaure, 1970; Turneaure, 1971; Grant et al., 1979, 1980; Lehmann et al., 1990). These deposits are spatially associated with metaluminous to peraluminous granitoids and subvolcanic stocks emplaced during two major metallogenic periods: (i) the Late Triassic - Early Jurassic that is restricted to the northern part of the belt; and (ii) the late Oligocene - early Miocene which affected the entire belt (Grant et al., 1979, 1980; Clark et al., 1983, 1990; McBride et al., 1983; Kontak et al., 1990a; Rice et al., 2005). In situ U-Pb cassiterite dating of ore deposits in the Bolivian tin belt (Gemmrich et al., 2021) confirms the earlier geochronological studies and indicates that Sn mineralization occurred at least during two major magmatic events in the Late Triassic (ca. 220-215 Ma) and in the late Oligocene - early Miocene (ca. 26-20 Ma). A significant Sn-Cu resource of similar age (~23 Ma) has been recently discovered 800 km north of San Rafael in the polymetallic deposit of Ayawilca (Benites et al., 2022).

San Rafael is currently one of the largest and highest-grade hypogene Sn deposits in the world, with total past production (1969-present) of more than 1 million metric tonnes (Mt) of Sn with an average grade of 3.7% (Harlaux et al., 2020). In 2020, total resources inventory of San Rafael was 195,300 t fine Sn in measured + indicated resources and 73,600 t fine Sn in

inferred resources, while total reserves were estimated at 132,000 t fine Sn (Minsur S.A., 2021). Ongoing exploration in the Nazareth zone, located about 3 km northeast of the San Rafael mine (Fig. 1B), reported 82,500 t fine Sn in measured + indicated resources and 82,050 t fine Sn in inferred resources (Minsur S.A., 2021). Therefore, a total of at least 565,450 t Sn in resources and reserves is known in the San Rafael district, accounting for a total of past production + remaining resources of >1.5 Mt Sn. The San Rafael deposit consists of a northwest-trending quartz-cassiterite-chlorite-sulfide vein system spatially associated with an uppermost Oligocene (ca. 24 Ma) peraluminous S-type, ilmenite-bearing granitic pluton exposed in a prominent topographic high (Nevado Quenamari, 5,300 masl). This domal feature is underlain by prehnite-pumpellyite facies metamorphosed and deformed Ordovician metasedimentary rocks of the Sandia Formation (Palma, 1981) which record a contact metamorphic aureole (Fig. 1B). The mineralized lodes at San Rafael were formed along fault-jogs created by sinistral-normal, strike-slip displacements (Mlynarczyk et al., 2003; Gialli et al., 2017). This extensional structural setting is interpreted, at the district scale, to have controlled the emplacement and uplift of the granitic pluton in a pull-apart system (Gialli et al., 2017).

The surface exposure of the San Rafael intrusive complex (SRIC) is dominated by a peraluminous S-type megacrystic biotite-cordierite monzogranite characterized by pluri-centimetric phenocrysts of K-feldspar (Figs. 2A and 3A) with lesser comagmatic enclaves of varied granitoids and subordinate lamprophyres (Kontak and Clark, 2002; Harlaux et al., 2021b). Other petrologic aspects of the SRIC which are relevant in the context of this study include: 1) whereas the bulk of the main intrusion constituting the SRIC is the aforementioned megacrystic facies, there are textural variants of this, namely a fine-grained granite that shows progressive gradual contacts toward the granitic cupola; 2) in the upper part of the intrusion, granophyric to graphic textures are noted; and 3) a variety of granitic phases and lamprophyres are observed deeper in the SRIC, such as comagmatic enclaves and dikes, demonstrating

commingling and mixing of felsic and mafic magma batches (Kontak and Clark, 2002; Harlaux et al., 2021b). Selected samples illustrating these features are provided in Appendix Figure A1 and the reader is referred to Harlaux et al. (2021b) for details. The SRIC has two major components, i.e., the San Rafael granite exposed in the southwestern part of the district and the Quenamari granite occurring in its northeastern part. Importantly, both bodies, which are discrete entities at surface, coalesce at depth as indicated by boreholes and underground workings (Fig. 1C). Furthermore, the SRIC is circumscribed by porphyritic ring dikes (RD on Fig. 1B), which are petrologically similar to the central granite (i.e., contain biotite ± cordierite) and exhibit quenched textures (Kontak and Clark, 2002). The southwestern tip of the San Rafael granite cupola is affected by greisenization at an elevation of >4,800 masl. The greisen occurs as an elongated body extending approximately 600 m in NNW-SSE direction close to the contact with the metasedimentary rocks of the Sandia Formation (Fig. 1B). This area is transitional to the megacrystic granite and consists of a quartz-muscovite greisen with minor tourmaline and dumortierite (Gialli et al., 2019; Harlaux et al., 2021b).

Analytical Methods

Petrography and automated mineralogy

Petrographic observations were carried out using transmitted-light microscopy combined with cold cathodoluminescence (CL) imaging to characterize the mineral textures. The CL images were acquired at the University of Geneva (Switzerland) using an Cathodyne® electron cathode from NewTec Scientific, mounted on a Olympus BX41 microscope operated with an acceleration voltage of 18 kV, a gun current of 120-200 µA, and with a processing resolution of 1,600 x 1,200 pixels. Automated mineral analysis and textural imaging of the samples were carried out using a FEI QEMSCAN Quanta 650 F facility at the University of Geneva. The

QEMSCAN system is equipped with two Bruker QUANTAX light-element energy-dispersive X-ray spectrometer (EDS) detectors. Analyses were conducted in field image operating mode at high vacuum (Pirrie et al., 2004), accelerating voltage of 25 kV, and using a beam current of 10 nA on carbon-coated polished thin sections. In total, 221 individual fields were measured per sample, with a field size of 1,500 x 1,500 µm, and a point spacing of 5 µm. The standard 1,000 counts per point were acquired, yielding a limit of detection of approximately 2 wt.% per element for mineral classification. Measurements were performed using the iMeasure v5.3.2 software, and the iDiscover v5.3.2 software package was used for data processing. Results consist of spatially resolved and fully quantified mineralogical maps and X-ray elemental distribution maps.

$^{40}Ar/^{39}Ar$ dating, Queen's University

Mineral separates of K-feldspar and mica (biotite, muscovite) prepared using conventional methods (i.e., crushing and sieving, magnetic separator, heavy liquids, handpicking) and flux monitors (standard LP-6 biotite: 128.1 ± 0.3 Ma; Baksi et al., 1996; 127.5 ± 0.3 Ma; Spell and McDougall, 2003; and internal standard SP-85 biotite: 18.9 ± 0.3 Ma; Quang et al., 2005) were wrapped in Al-foil and together loaded into a radiation canister and irradiated with fast neutrons in position 5C of the McMaster University nuclear reactor (Hamilton, Ontario, Canada) for 20 hours. The standards were evenly spaced with the unknowns to enable precise determination of the irradiation parameter *J* throughout the canister. Approximately 250-300 mg of sample material was loaded into degassed (1200°C) Nb crucibles and placed in a quartz tube connected to a stainless-steel extraction system and step-heated using a Lindberg furnace. Argon isotopes were measured at Queen's University (Kingston, Canada) using a bakeable, ultra-high vacuum, stainless-steel Ar extraction system operated on-line to a substantially modified, A.E.I. MS-10 mass spectrometer which was run in the static mode. Measured Ar isotope ratios were

extrapolated to zero-time and corrected for neutron-induced ^{40}Ar from K, and ^{39}Ar and ^{36}Ar from Ca. The atmospheric $^{40}Ar/^{36}Ar$ ratio was measured regularly, and appropriate corrections were applied. Ages (i.e., plateau, correlation, and integrated) and uncertainties were calculated using IsoplotR (Vermeesch, 2018) and the decay constants and isotope abundance ratios recommended by Steiger and Jäger (1977). An additional component of uncertainty is introduced by inhomogeneity of the reference material LP-6 biotite, as reported by Spell and McDougall (2003). The full Ar isotope dataset is presented in Appendix Table A1.

$^{40}Ar/^{39}Ar$ dating, University of Geneva

Mineral separates of adularia were concentrated from representative splits of the crushed rocks using magnetic and heavy liquid separation techniques and finally handpicked (~99.9% purity) under a binocular microscope. Adularia concentrates were rinsed in deionized water, packed in copper foil and irradiated in the CLICIT facility of the TRIGA reactor at Oregon State University (USA) for 3.5 hours. Fish Canyon Tuff sanidine (Kuiper et al., 2008) was used to monitor neutron fluxes. Samples were degassed by step-heating with a 55W CO_2-IR laser (Photon Machines Inc.) that was rastered over the samples to provide even-heating of the grains, and the extracted gas was gettered (SAES GP50 ST101 and AP10) in a stainless steel UHV line, after passing through a cold trap chilled to ~150 K. Argon isotopes were analyzed at the University of Geneva using a multi-collector GV Instruments Argus V mass spectrometer equipped with four high-gain (10^{12} Ω) Faraday detectors, and a single 10^{11} Ω Faraday detector (^{40}Ar), with a procedure identical to that described in Villagomez and Spikings (2013). Time-zero regressions were fitted to data collected from twelve cycles. Data reduction and calculation of age plateaus were performed utilizing ArArCalc (Koppers, 2002) and IsoplotR (Vermeesch, 2018). Blank measurements were made after every three step analyses, and mass discrimination

was determined from analyses of gettered air, which were made daily. The full Ar isotope dataset is presented in Table A2.

U-Pb dating of cassiterite, USGS Denver

U-Pb isotope analyses of cassiterite were conducted at the United States Geological Survey (USGS) Denver Science Federal Center (USA), G3 Plasma Laboratory using a Nu Instruments AttoM™ sector-field inductively coupled plasma – mass spectrometer (ICP-MS) coupled to a Teledyne-Photon Machines Excite™ 193 nm ArF excimer laser system with a HelEx II 2-volume ablation cell. Polished thin sections of cassiterite and standard reference materials NIST-610 and NIST-612 glass were ablated using spot mode (150 total bursts) with a repetition rate of 5 Hz, laser energy of 3-5 mJ, and an energy density of 4-5 J/cm^2. The rate of He gas flow to the HelEx cell of the laser was ~0.5 L/min and make-up Ar gas (0.21-0.29 L/min) was added to the sample stream prior to introduction into the plasma. Nitrogen, with flow rate of 5.5-6.0 mL/min, was added to the sample stream, which allowed for significant reduction in oxide formation (monitored during the mass spectrometer tuning) to obtain ThO^+/Th^+ (<0.5%) and improved the ionization efficiency of refractory Th (Hu et al., 2008). With the magnet parked at a constant mass, flat tops of the isotope peaks were measured at the following masses by rapidly deflecting the ion beam: ^{202}Hg, ^{204}(Hg+Pb), ^{206}Pb, ^{207}Pb, ^{208}Pb, ^{232}Th, ^{235}U, and ^{238}U. On-peak backgrounds for each peak were measured for 30 s prior to each 30 s analysis. A discrete dynode electron multiplier ion-counting detector was always used operating below the limit of the ion beam attenuation (<2.5×10^6 cps). Raw data were reduced off-line using the Iolite™ 2.5 program and U_Pb_Geochronology3 Data Reduction Scheme (Paton et al., 2011) to subtract on-peak background signals, correct for Pb isotope fractionation and U-Pb downhole fractionation, normalize the instrumental mass bias, and determine the concentration of U, Pb, and Th. NIST-610 glass standard was analyzed in each session to evaluate U and Th

concentrations. A laser spot size of 85-110 µm was used. Pit depths of ~9-10 µm resulted in pit aspect ratios (diameter/depth) of >5 so that downhole U/Pb fractionation is minimized. An ~1.54 Ga low-Th cassiterite sample (named "SPG-IV") from a mineralized skarn in Russian Karelia with an apparently closed U-Pb system was analyzed during each analytical session (five analyses after five unknowns) as a matrix-matched reference material (Neymark et al., 2018). NIST-612 (two analyses after five unknowns), the cassiterite reference material (SPG-IV), and the cassiterite unknowns are all analyzed under the same conditions during each analytical session.

Data reduction for cassiterite is complicated by the presence of variable amounts of common Pb and the absence of a well-characterized matrix-matched cassiterite reference material. To avoid these complications, Neymark et al. (2018) developed a novel approach that does not require an ID-TIMS characterized reference material; this approach was adopted for this study. Using normalization to the $^{238}U/^{206}Pb$ and $^{207}Pb/^{206}Pb$ isotopic ratios of NIST-612, biased lower intercept U-Pb isotopic dates were calculated for the ~1.54 Ga SPG-IV cassiterite measured in the same analytical sessions as unknowns by constructing a Tera-Wasserburg isochron diagram. The measured long-term average $^{207}Pb/^{206}Pb$ date of more than 100 replicate LA-ICP-MS analyses of this cassiterite is 1541.2 ± 9.5 Ma (2SD), which is within uncertainty of the recently published ID-TIMS age for this sample of 1535.9 ± 5.5 Ma (Tapster and Bright, 2020). The difference between the biased lower intercept U-Pb date and the obtained $^{207}Pb/^{206}Pb$ date of the cassiterite reference material SPG-IV is used to correct for the matrix effect and the instrumental bias on $^{238}U/^{206}Pb$ ratios. A more detailed discussion of the analytical and data reduction methods can be found in Neymark et al. (2018). The full U-Pb isotope dataset of cassiterite, including results on cassiterite SPG-IV, is presented in Table A3. Data were plotted using IsoplotR (Vermeesch, 2018), and uncertainties in tables and text are quoted at the 2σ level.

Major and trace element analysis of cassiterite

The major element composition of cassiterite was determined by electron microprobe analyses (EMPA) using a JEOL JXA-8200 Superprobe microanalyzer equipped with five wavelength-dispersive X-ray spectrometers (WDS) at the University of Geneva. Operating conditions were as follows: acceleration voltage of 20 kV, beam current of 20 nA, and beam diameter of 5 μm. Analytical standards, with the corresponding lines, and limits of detection used for analyses, were: SnO_2 (Sn, Lα, 150 ppm), TiO_2 (Ti, Kα, 110 ppm), $MnTiO_3$ (Mn, Kα, 100 ppm), Ta_2O_5 (Ta, Lα, 350 ppm), Nb_2O_5 (Nb, Lα, 200 ppm), Fe_2O_3 (Fe, Kα, 100 ppm), W-metal (W, Lα, 150 ppm), and In-metal (In, Lα, 150 ppm). Chemical compositions of cassiterite are reported in weight per cent (wt.%) oxides and structural formulae, normalized to two oxygen atoms, are expressed in atoms per formula unit (apfu). Results of EMPA measurements are reported in Table A4.

Cassiterite trace element analyses were carried out at the ETH Zürich (Switzerland) by LA-ICP-MS using a RESOlution (Australian Scientific Instruments) 193 nm ArF excimer laser system attached to an Element XR (Thermo Scientific, Germany) sector-field mass spectrometer. Analyses were performed on the same polished thin sections of cassiterite prior to the U-Pb isotope analyses at the USGS. Samples were loaded in a Laurin Technic S-155 dual-volume ablation cell fluxed with carrier gas consisting of ca. 0.5 L/min He (5.0 grade) and sample gas from the ICP-MS consisting of ca. 1 L/min Ar (6.0 grade) mixed with ca. 2 mL/min N_2. We used a laser repetition rate of 3 Hz, spot diameters of 43 μm, and a laser output energy of ca. 40 mJ, corresponding to an on-sample energy density of ca. 3.6 J/cm^2. Three pre-ablation pulses were applied immediately before each analysis for surface cleaning. Signal homogenization was performed using in-house Squid tubing. The ICP-MS was tuned for maximum sensitivity on the high mass range while keeping the production of oxides low

($^{248}ThO^+/^{232}Th^+ \approx 0.10\%$, $Ba^{2+}/Ba^+ \approx 3.5\%$). Intensities for the 45 following isotopes were acquired using time resolved-peak jumping and triple detector mode: ^{27}Al, ^{29}Si, ^{45}Sc, ^{49}Ti, ^{51}V, ^{53}Cr, ^{55}Mn, ^{57}Fe, ^{65}Cu, ^{66}Zn, ^{71}Ga, ^{74}Ge, ^{75}As, ^{89}Y, ^{90}Zr, ^{93}Nb, ^{95}Mo, ^{107}Ag, ^{111}Cd, ^{113}In, ^{117}Sn, ^{139}La, ^{140}Ce, ^{141}Pr, ^{145}Nd, ^{147}Sm, ^{153}Eu, ^{157}Gd, ^{159}Tb, ^{163}Dy, ^{165}Ho, ^{167}Er, ^{169}Tm, ^{173}Yb, ^{175}Lu, ^{178}Hf, ^{181}Ta, ^{186}W, ^{206}Pb, ^{207}Pb, ^{208}Pb, ^{232}Th, and ^{238}U. Dwell times were set to 10 ms, except for ^{27}Al, ^{29}Si, ^{45}Sc, ^{49}Ti, and ^{51}V (5 ms), ^{57}Fe, ^{117}Sn, and ^{186}W (11 ms), all REEs, ^{206}Pb, and ^{207}Pb (15 ms). With these settings, the total sweep time was about 760 ms. Each measurement consisted of 30 s of gas blank measurement followed by 30 s of sample ablation.

The raw intensities were processed using the Matlab-based SILLS software (Guillong et al., 2008). The analyzed In intensities on mass 113 were corrected for interferences by subtracting the contribution of ^{113}Cd based on the measured ^{111}Cd intensities and using natural isotope ratios for Cd recommended by IUPAC. Individual LA-ICP-MS spectra were checked for possible presence of micro-inclusions whereas spikes unrelated to the analyzed sample were systematically eliminated. Integration windows were defined only for plateau-like signals thus avoiding parts of the sample signal contaminated by the matrix or micro-inclusions. NIST-612 glass (Jochum et al., 2011) was used as a primary reference material (analyzed with a spot diameter of 43 µm) for trace element quantification using as an internal standard the wt.% Sn content determined by EMPA. Repeated analyses of USGS glass reference materials (GSD-1G and BHVO-2G; Guillong et al., 2005) were processed as unknowns with laser spot diameter of 43 µm to check accuracy and reproducibility of the analyses. Results show that reproducibility ranges from 3 to 12% (2SD, increasing with decreasing concentration) for all analyzed trace elements, and that the analyses are accurate within this level of analytical uncertainty. Limits of detection (LOD) were calculated using the equation of Pettke et al. (2012) and are reported together with the trace element dataset in Table A5.

Revised Paragenetic Sequence of the San Rafael Deposit

Based on new petrographic observations and building on previous work (Palma, 1981; Kontak and Clark, 2002; Mlynarczyk et al., 2003; Mlynarczyk and Williams-Jones, 2006; Wagner et al., 2009; Corthay, 2014; Prado Flores, 2015; Gialli et al., 2019; Harlaux et al., 2020, 2021b, 2021c; Cazorla Martínez, 2022), we propose a revised paragenetic sequence for the San Rafael Sn (-Cu) deposit that is divided into five main stages (Fig. 4):

Pervasive alkali metasomatism (stage 0)

Granitic rocks composing the SRIC are widely affected by pervasive alkali metasomatism that occurred during cooling of the pluton and represents the earliest hydrothermal alteration recognized at San Rafael, mainly in the upper 500 m of the intrusive complex. This event consists of potassic alteration of the granitic groundmass resulting in partial replacement of igneous plagioclase and perthitic K-feldspar phenocrysts by discrete patches of hydrothermal Ba-rich K-feldspar, initially along fractures and grain boundaries (Kontak and Clark, 2002). Subsequently, the granitic rocks were affected by pervasive sodic alteration which represents the dominant subsolidus alteration in the deepest parts of the SRIC (Gialli et al., 2019). Sodic alteration resulted in hydrothermal albite which selectively replaced and formed overgrowths on magmatic K-feldspars (i.e., “pseudo-rapakivi” texture according to Kontak et al., 1984). Nevertheless, it is still unclear whether these observations reflect a temporal decoupling of Na alteration overprinting previous K alteration, or a vertical zonation of alkali metasomatism at the pluton scale. QEMSCAN mineral maps illustrating this early pervasive (K)-Na metasomatism are provided in Figure A2.

Greisenization and quartz-tourmaline veining/brecciation (stage I)

Alkali metasomatism of the granitic pluton was followed by the emplacement of pre-ore quartz-tourmaline veins and breccias, which cut the multiple phases of the SRIC and the metasedimentary host rocks (Fig. 2C). The emplacement of quartz-tourmaline veins was preceded by or was synchronous to the development of a quartz-muscovite greisen, which crops out in the southwestern part of the San Rafael granite (Fig. 1; Harlaux et al., 2021b) and along the contact between the megacrystic granite and the hornfelsed phyllites (Palma, 1981). Temporal relationships between alkali metasomatism and greisenization are unclear, but we propose that greisen formation postdated (K)-Na alteration based on the lack of hydrothermal albite overprinting the greisen and the local development of greisen alteration halos along the early quartz-tourmaline veins crosscutting the metasomatized granitic rocks. The greisen consists dominantly of a quartz-muscovite assemblage (>95% rock volume) containing sparse patches of tourmaline and dumortierite (Figs. 2B-3B and A3). Locally, holtite that replaced dumortierite was identified by optical microscopy and Raman spectroscopy (Fig. A3). Most of the major magmatic minerals (plagioclase, K-feldspar, biotite, cordierite) are altered, except for quartz and rare residual feldspars. In addition, the primary igneous texture, excepting that of the primary quartz, is destroyed. Field observations show that the intensity of greisenization varies spatially and increases progressively towards the upper part of the granitic stock, which suggests ponding of orthomagmatic fluids during cooling of the San Rafael pluton. The quartz-tourmaline veins, mostly subvertical and narrow (<2 cm wide), are commonly rimmed by alteration halos of variable thickness dominantly composed of hydrothermal albite (Figs. 2C and 3C). Based on rock staining and QEMSCAN imaging (Kontak and Clark, 2002; Gialli et al., 2019), this vein-restricted Na alteration is interpreted to accompany the development of the quartz-tourmaline veins as the fluids were progressively neutralized during interactions with the host granitic rocks. Lastly, arsenopyrite is found in the quartz-tourmaline veins/breccias with minor amounts of löllingite and hexagonal pyrrhotite, a mineral assemblage that is

characteristic of low-sulfidation conditions (Einaudi et al., 2003). Accessory apatite and rutile are also observed in the quartz-tourmaline veins and breccias. There are several macroscopic- and microscopic-scale observations that suggest that the fluids related to this tourmaline stage infiltrated large amounts of the SRIC (Kontak and Clark, 2002; Mlynarczyk and Williams-Jones, 2006; Harlaux et al., 2020): 1) presence of radial tourmaline pseudomorphs after K-feldspar megacrysts; 2) variable development of disseminated tourmaline in the granitic groundmass throughout the SRIC; and 3) widespread occurrence of secondary fluid inclusions in magmatic quartz phenocrysts. These fluid inclusions include two-phase liquid-rich inclusions (L-V) with vapor phase <30%, two-phase vapor-rich inclusions (V) containing >80% vapor, and hypersaline multiphase inclusions (L-V-H) containing halite, sylvite, and other solids. Notably, whereas the L-V types are similar to those observed in the ore stages, the other two are only seen in the early quartz-tourmaline stage (Palma, 1981; Kontak and Clark, 2002; Wagner et al., 2009; Cazorla Martínez, 2022).

Main cassiterite ore mineralization (stage II)

The main Sn-ore assemblage is formed during this stage and consists dominantly of quartz, cassiterite, and chlorite, with minor tourmaline in veins and breccias that locally reopened pre-existing quartz-tourmaline veins. Tin mineralization occurs either as botryoidal cassiterite ("wood tin"; Figs. 2D and 3D) or as coarse-grained cassiterite (Figs. 2E and 3E), which are both intimately intergrown with chlorite and quartz (Kontak and Clark, 2002; Mlynarczyk et al., 2003; Corthay, 2014; Prado Flores, 2015). This stage is associated with an intense, pervasive development of chlorite along veins and breccia bodies and affected both the granitic stock and the metasedimentary host rocks. Hydrothermal breccias contain clasts of chloritized wall rocks cemented by quartz with both botryoidal and coarse-grained cassiterite. The complicated textures of the Sn-rich breccias indicate that this stage was not a single

hydrothermal event, but instead consisted of episodic sealing and reopening producing characteristic textures of alternating cassiterite, chlorite, and quartz layers. Very minor wolframite and scheelite have been reported in some mineralized lodes (Kontak and Clark, 2002; Mlynarczyk et al., 2003). Locally, the terminal end of this stage overlaps with the stage III base-metal deposition and is best represented by the presence of alternating layers of wood tin and sphalerite.

Polymetallic sulfide and cassiterite mineralization (stage III)

During stage III, a polymetallic sulfide-dominant assemblage with abundant quartz and chlorite was deposited (Figs. 2F-3F). It occurs as quartz-chlorite-sulfide veins and breccias and as a late infill that cuts and reopened pre-existing vein generations. Sulfides include chalcopyrite, pyrite, galena, and sphalerite intergrown with lesser cassiterite and minor pyrrhotite, arsenopyrite, stannite, marcasite, native bismuth, acanthite, and various accessory sulfosalts (e.g., matildite, aleksite, kobellite, fahlore; Kontak and Clark, 2002; Corthay, 2014; Prado Flores, 2015). Additional minerals of this stage include adularia (low-sanidine structure), fluorite, siderite, and ankerite. Stage III cassiterite was initially reported to occur as predominantly fine-grained acicular ("needle tin") in direct association with quartz, chlorite, chalcopyrite, and pyrite assemblages (Kontak and Clark, 2022; Fig. 3F). New observations in the deepest parts of the San Rafael deposit show that coarsely crystalline cassiterite was also deposited together with the full range of base metal sulfides and that, moreover, cassiterite deposition persisted locally after sulfide formation. Thus, cassiterite, either as coarse-grained or acicular in texture, was deposited during stage III, contrasting significantly with botryoidal cassiterite that is only restricted to the sulfide-absent stage II. Deposition of adularia and Fe-carbonates (siderite, ankerite) locally postdated that of base metal sulfides and cassiterite.

Quartz-carbonate veining (stage IV)

Late quartz-carbonate (mainly calcite and siderite) veins, with variable amounts of fluorite, adularia, chlorite, and Sb-Fe-Ni sulfides and sulfosalts (stibnite, gudmundite, and mackinawite), cut all previous veins and breccias and locally directly overprints the stage III quartz-sulfide assemblage (Figs. 2F and 3F), indicating a continuous depositional sequence (Kontak and Clark, 2002; Corthay, 2014; Prado Flores, 2015). Late rhodonite-johannsenite veins and breccias locally cut early quartz-base metal sulfide veins in the Quenamari area (Corthay, 2014), and they are thought to represent a later high-temperature hydrothermal event. Interestingly, the Quenamari Mn-rich occurrence is close to the now inactive, Minastira Mn deposit, which is situated adjacent to a small plug of cordierite-biotite megacrystic monzogranite (Clark et al., 1990).

Sample Description and Characterization

We have selected both magmatic (biotite, K-feldspar) and hydrothermal (muscovite, adularia, cassiterite) minerals to ascertain the lifetime of the ore-forming magmatic-hydrothermal system at San Rafael. Sample description, location, and ages are summarized in Table 1 and macroscopic (i.e., slab pictures) and microscopic (i.e., thin section scans) images of most of the dated samples in this study are provided in Figures A4 to A7.

Magmatic biotite and K-feldspar phenocrysts

Eight biotite phenocrystic separates were prepared from the cordierite-bearing K-feldspar megacrystic granite of the SRIC, including five samples from San Rafael (COCA-150, COCA-151, COCA-166A, COCA-408, COCA-1800) and three samples from Quenamari (COCA-194, COCA-197, COCA-244). Images showing the various nature of dated biotite samples are

449 provided in Figures A4-A5 as thin section scans and higher magnification images. Notably the
450 finer-grained, but also quartz-K-feldspar-cordierite-phyric, dike samples rarely had sufficient
451 and/or fresh biotite suitable for $^{40}Ar/^{39}Ar$ dating. The single biotite sample (COCA-249) from
452 a porphyritic ring dike, west of the San Rafael granite (Kontak and Clark, 2002), that was
453 nonetheless processed for $^{40}Ar/^{39}Ar$ dating returned an irregular age spectrum, with no plateau
454 that is suitable for age interpretation; for this reason, the data are not reported here. The other
455 biotite separates used for dating, which come from weakly to moderately altered granites (see
456 Table 1 and Fig. A5), are of millimetric size and their chemical composition, as determined
457 from EMPA, is reported in Kontak and Clark (2002). Samples COCA-194 and COCA-1800
458 are the least altered of those dated. Whereas the former is from the main lode of the Quenamari
459 granite, the latter was taken in the 4,200 masl adit that crosscuts the same granite. The location
460 of this sample, approximately in the upper part of the main stock, is about 15 m E-NE of the
461 projected downward extension of the Jorge vein. It appeared free of hydrothermal alteration
462 and the cordierite was about 80% translucent, with only marginal pinitization.

463 Four samples of magmatic, megacrystic K-feldspar were used for $^{40}Ar/^{39}Ar$
464 geochronology (Table 1). Two samples (COCA-165B and COCA-408A) are from the least
465 altered San Rafael cordierite-biotite megacrystic granite whereas the two other samples
466 (COCA-190 and COCA-198) are from K-feldspar porphyritic ring dikes east of the Quenamari
467 granite at an elevation of ca. 4,800-4,845 masl (see Kontak and Clark, 2002 for locations). Bulk
468 analysis (reported as mol.% Or) of these samples yielded: COCA-165B = Or_{88}, COCA-408A =
469 Or_{76}, COCA-190 = Or_{93}, COCA-198 = Or_{85} (Kontak and Clark, 2002). Importantly, earlier
470 detailed crystallographic and geochemical studies of the megacrystic K-feldspar phase, from
471 both the main intrusive and ring dikes of the SRIC, were undertaken to investigate the cooling
472 history of the magmatic phases in addition to the influence of overprinting hydrothermal
473 activity (i.e., metasomatism) on these rocks (Kontak et al., 1984; Kontak and Clark, 2002). We

summarize below and in Figure 5 the results of the aforementioned crystallographic work, in addition to further results from Kontak (1985), along with relevant petrographic observations in Figure A6. This information is relevant in the context of this study to interpret the $^{40}Ar/^{39}Ar$ age spectra for the K-feldspar separates.

X-ray diffraction (XRD) provides insight into Al-Si ordering/disorder relationships in alkali feldspars, their chemical composition, and indirectly the nature of fluids in plutons; thus, feldspars have long been a subject of study (e.g., Wright, 1968; Parsons, 1978). The following points are noted for studied samples from the SRIC: 1) overall K-feldspar from the Quenamari dike rocks retain a less ordered structure (i.e., intermediate between sanidine and orthoclase) than those hosted in the coarse-grained granites in both settings that are dominated by orthoclase. For comparison, data for K-feldspar megacrysts from a similar, in age (ca. 25 Ma) and composition, felsic dike at nearby Antauta (ca. 12 km south; Kontak et al., 1987) is also shown in Figure 5. As noted in the latter figure, some of the K-feldspar from dikes at Quenamari retain a highly disordered structure; 2) overall the K-feldspars are unmixed and retain primary magmatic compositions of about $Or_{75}Ab_{25}$, as inferred from their position in the XRD plot, which is further confirmed from the very minor 201 albite reflects in the XRD patterns, bulk analyses of mineral separates, EMPA analyses (Kontak and Clark, 2002), and petrography (see below); and 3) where metasomatism has occurred, the chemistry of the K-feldspar has changed to near end-member K-feldspar (i.e., Or_{100}). This process was heterogeneous, in some cases affecting entire rocks whereas in others only parts of crystals, which again has been confirmed through both bulk and in situ analyses (Kontak and Clark, 2002). Although not shown in Figure 5, the development of albite commensurate with sodic metasomatism was also documented by the previous XRD and chemical studies, the latter showing that the primary plagioclase of An_{20-40} was converted to An_0 during its subsolidus transformation. These features revealed through XRD studies are also seen at both macro- and microscopic scales, indicating that K-feldspar

megacrysts were dominated by cryptoperthite and film perthite in least altered rocks (Figs. A1 and A6). However, these latter areas are either replaced by or traversed by discordant vein-like networks characterized by flame and blebby perthite and turbidity owing to the abundance of fluid inclusions, thus representing evidence of where coupled dissolution-reprecipitation processes have locally reconstituted the feldspar (e.g., Putnis, 2002, 2009; Plümer and Putnis, 2009). Also significant is the local development of adularia-like veinlets with up to 6 wt.% BaO that cut areas of pitted orthoclase (Fig. A6; see Kontak and Clark, 2002 for details).

Hydrothermal muscovite and adularia

Three samples of coarse-grained muscovite were collected from greisenized areas to constrain the timing of the early hydrothermal alteration of the SRIC concomitant with the formation of pre-ore quartz-tourmaline veins and breccias (stage I). Sample COCA-247 was collected from a quartz-muscovite-dumortierite-tourmaline greisen bordering a quartz-tourmaline vein in the megacrystic granite at San Rafael at an elevation of ca. 4,970 masl (see descriptions in Kontak, 1985; Kontak et al., 1987; and Fig. A3). Sample SARL-406 was collected from a muscovite-rich alteration zone affecting the megacrystic granite, interpreted to be related to a greisen-like alteration, and contiguous with the San Rafael lode on the level 4,770 masl (Palma, 1981). Sample SARL-486 originates from a muscovite-rich alteration zone in the hornfelsed phyllites in the immediate vicinity of the contact with the megacrystic granite along the road leading to the level 4,820 masl (see Palma, 1981 for descriptions). In this location, the metasedimentary rocks are cut by a steeply dipping hydrothermal breccia containing angular to rounded clasts of quartzitic rocks and coarse-grained granite within a fine-grained muscovite-rich matrix, interpreted as an exogreisen overlying the apex of the granitic intrusion. The three aforementioned samples are thought to be representative of the greisenization event following

the crystallization of the granitic pluton and contemporaneous with the emplacement of stage I quartz-tourmaline veins.

Three samples of adularia were selected to date the hydrothermal stages III and IV. Sample SARL-434 was collected at the northwestern end of the 820 adit on the Jorge lode in the level 4,820 masl of the San Rafael mine (Palma, 1981). This sample consists of a massive milky-white adularia intergrown with quartz and associated with a stage III base-metal sulfide assemblage composed of chalcopyrite, sphalerite, galena, and chlorite. Two additional adularia samples (SRG-43 and SR-16-KK-02; Fig. A6) were collected from stage IV quartz-adularia±fluorite veins hosted in the Sandia metasedimentary rocks in the metamorphic contact aureole of the SRIC. Sample SRG-43 was collected from the Alejandrina vein crosscutting metasedimentary rocks in the Quenamari area east of the contact with the megacrystic granite at ca. 4,920 masl. The sample has millimetric milky-white adularia intergrown with a quartz-fluorite assemblage coring a re-opened chlorite-chalcopyrite vein from stage III. Sample SR-16-KK-02 is from the Estancococha area located east of the San Rafael granite at an elevation of ca. 4,720 masl. This sample is composed of millimeter-thick quartz-adularia veinlets crosscutting andalusite-bearing metasedimentary rocks. The adularia forms an aggregate of milky-white, millimeter-sized grains intergrown with quartz. Field relationships and the absence of chlorite and sulfides suggest that adularia crystallized during a later, essentially post-sulfide, hydrothermal stage.

Hydrothermal cassiterite

We selected four samples of cassiterite representative of the main ore stage II that were collected in different underground levels of the San Rafael mine. Photographs of the cassiterite samples at macroscopic and microscopic scales are provided in Figure A7. Sample SRG-62-1, from the San Rafael lode in the level 4,310 masl, consists of botryoidal cassiterite ("wood tin")

intergrown with chlorite and quartz that is cut by quartz-pyrite±chalcopyrite veins of stage III. In transmitted light, cassiterite is dark brown to yellow and forms laminated bands ca. 100 to 500 µm thick. Sample SR-16-KK-14 is from a dilational jog in a historical bonanza ore body in the San Rafael lode (ca. 4,400 masl) and consists of massive wood tin, chlorite, and quartz coating breccia clasts, hence representing classical San Rafael ore (e.g., Mlynarczyk et al., 2003). This cassiterite is also banded and forms 100-300 µm-thick laminations of light to dark brown color in transmitted light. Sample COCA-80-1 comes from the historical San Rafael lode in the upper part of the mine (4,533 masl) and corresponds to wood tin intergrown with chlorite and quartz in typical breccia from the high-grade Sn ore zone. It is in many respects similar to sample SR-16-KK-14 described above. Sample SRG-95, from the Kimberly vein on the level 3,950 masl near the San Rafael vein, corresponds to coarse-grained cassiterite in quartz-chlorite veins with an open-space texture. The cassiterite grains range in size from <100 µm to a few millimeters and show primary growth zoning in transmitted light with light yellow to brown colors.

Results

Biotite $^{40}Ar/^{39}Ar$ geochronology

The results of $^{40}Ar/^{39}Ar$ dating for magmatic biotite from the megacrystic biotite-cordierite granite of the SRIC are reported in Table A1 with the age spectra shown in Figures 6 and 7. Two groups of biotite samples are distinguished based on their Ar release spectra. The first group (Fig. 6) includes samples COCA-166A, COCA-194, COCA-244 and COCA-1800, which are all characterized by at least five consecutive steps accounting for >50% of the ^{39}Ar released with no slope, and have Mean Square Weighted Deviation (MSWD) values ≈ 1, thus representing plateaus as defined by Schaen et al. (2021). Sample COCA-166A (~6.5 wt.% K)

yields a plateau date of 24.29 ± 0.26 Ma (2σ) for 78% of the released ^{39}Ar, which is consistent with the inverse isochron date of 24.32 ± 0.30 Ma (2σ; MSWD = 1.9; Fig. 6A). Sample COCA-194 (~7.0 wt.% K) is characterized by a plateau date of 24.35 ± 0.28 Ma (2σ), which includes 99% of the released ^{39}Ar and overlaps the inverse isochron date of 24.32 ± 0.30 Ma (2σ; MSWD = 1.7; Fig. 6B). Sample COCA-244 (~6.8 wt.% K) gives a plateau date of 24.52 ± 0.28 Ma (2σ) including 99% of the released ^{39}Ar and yields an inverse isochron date of 24.46 ± 0.30 Ma (2σ; MSWD = 0.7; Fig. 6C). Sample COCA-1800 (~7.3 wt.% K) yields a plateau date of 24.10 ± 0.26 Ma (2σ), including 99% of the released ^{39}Ar, which is consistent with the inverse isochron date of 24.04 ± 0.28 Ma (2σ; MSWD = 0.8; Fig. 6D).

The second group of biotite samples (Fig. 7), which includes COCA-150, COCA-151, COCA-197 and COCA-408, is characterized by slight discordance and minor hump-shaped or staircase patterns with MSWD values >> 1. Sample COCA-150 (~6.5 wt.% K) shows a staircase upward pattern with younger apparent dates calculated for the initial heating steps; it yielded an inverse isochron date of 24.90 ± 0.30 Ma (2σ; MSWD = 42; Fig. 7A). Sample COCA-151 (~6.6 wt.% K) shows a staircase downward pattern with high-temperature heating steps trending towards younger apparent dates; it yielded an inverse isochron date of 24.50 ± 0.30 Ma (2σ; MSWD = 8.2; Fig. 7B). Sample COCA-197 (~6.8 wt.% K) shows a slight hump-shaped spectrum with one high-temperature step giving an older apparent date; it yielded an inverse isochron date of 24.70 ± 0.30 Ma (2σ; MSWD = 22; Fig. 7C). Sample COCA-408 (~7.1 wt.% K) is characterized by a staircase downward pattern with high-temperature heating steps trending towards younger apparent dates; it yielded an inverse isochron date of 24.80 ± 0.40 Ma (2σ; MSWD = 9.0; Fig. 7D).

K-feldspar ^{40}Ar/^{39}Ar geochronology

The results of $^{40}Ar/^{39}Ar$ dating of magmatic K-feldspar from the megacrystic granite are reported in Table A1 and age spectra are shown in Figure 8. In addition, the Al-Si ordering for these samples is summarized in Figure 5. All K-feldspar samples show disturbed $^{40}Ar/^{39}Ar$ incremental heating spectra with quasi-U-shaped patterns. Sample COCA-165B (~88 mol.% Or) yielded $^{40}Ar/^{39}Ar$ apparent dates between ca. 33.6 Ma and ca. 22.4 Ma but defines low- and high-temperature pseudo-plateaus dates of 22.50 ± 0.40 Ma and 24.20 ± 0.40 Ma, respectively (2σ; Fig. 8A). Sample COCA-190 (~93 mol.% Or) yielded $^{40}Ar/^{39}Ar$ apparent dates ranging from ca. 31.5 Ma to ca. 23.0 Ma, but also defines low- and high-temperature pseudo-plateaus dates of 23.15 ± 0.40 Ma and 24.15 ± 0.40 Ma, respectively (2σ; Fig. 8B). Sample COCA-198 (~85 mol.% Or) yielded $^{40}Ar/^{39}Ar$ apparent dates ranging from ca. 31.6 Ma to ca. 22.3 Ma, and again defines low- and high-temperature pseudo-plateau dates of 22.80 ± 0.40 Ma and 24.15 ± 0.40 Ma, respectively (2σ; Fig. 8C). Sample COCA-408A (~76 mol.% Or), which interestingly has the most disordered structure of the dated K-feldspar samples (Fig. 5), yielded $^{40}Ar/^{39}Ar$ apparent dates between ca. 34 Ma and ca. 11.6 Ma, defining low- and high-temperature step dates of 23.70 ± 0.40 Ma and 26.50 ± 0.40 Ma, respectively (2σ; Fig. 8D).

Muscovite and adularia $^{40}Ar/^{39}Ar$ geochronology

The $^{40}Ar/^{39}Ar$ dating of the hydrothermal stages I to IV is based on three muscovite and three adularia samples. The relevant data are reported in Tables A1 and A2 with the respective age spectra shown in Figures 9 and 10. All samples show at least five consecutive steps defining plateaus with MSWD values ≈ 1.

Coarse-grained muscovite sample COCA-247 (~6.8 wt.% K) from a stage I greisen bordering a quartz-tourmaline vein yielded a plateau date of 24.18 ± 0.24 Ma (2σ) representing 99% of the released ^{39}Ar, which overlaps the inverse isochron date of 24.21 ± 0.28 Ma (2σ; MSWD = 1.8; Fig. 9A). In comparison, muscovite sample SARL-406 (~7.5 wt.% K), which

622 comes from a greisen-bordered mineralized vein, yielded a plateau date of 24.36 ± 0.24 Ma
623 (2σ) for about 82% of the released ^{39}Ar and overlaps the inverse isochron date of 24.55 ± 0.50
624 Ma (2σ; MSWD = 1.2; Fig. 9B). Sample SARL-486 (~6.9 wt.% K), collected from an
625 exogreisen muscovite-rich zone in the quartzitic metasedimentary host rocks, yielded a plateau
626 date of 24.19 ± 0.24 Ma (2σ) for about 90% of the released ^{39}Ar and an inverse isochron date
627 of 24.20 ± 0.50 Ma (2σ; MSWD = 4.5; Fig. 9C).

628 Adularia sample SARL-434 (~11.5 wt.% K), which is associated with the polymetallic
629 stage III, yielded a plateau date of 22.29 ± 0.24 Ma (2σ) for 94% of the released ^{39}Ar and is
630 consistent with the inverse isochron date of 22.32 ± 0.40 Ma (2σ; MSWD = 1.9; Fig. 10A). The
631 adularia sample SRG-43 (~14.5 wt.% K), which comes from the post-ore stage IV, yielded a
632 plateau date of 22.72 ± 0.11 Ma (2σ) for about 96% of the released ^{39}Ar and overlaps the inverse
633 isochron date of 22.83 ± 0.28 Ma (2σ; MSWD = 1.4; Fig. 10B). Lastly, adularia sample SR-16-
634 KK-02 (~15.1 wt.% K), which is also from the post-ore stage IV, yielded a plateau date of 22.43
635 ± 0.16 Ma (2σ) for 99% of released ^{39}Ar and overlaps with the inverse isochron date of 22.33
636 ± 0.21 Ma (2σ; MSWD = 2.1; Fig. 10C).

637

638 *Cassiterite U-Pb geochronology*

639 U-Pb isotopic analyses of cassiterite are presented in Table A3 and illustrated on Tera-
640 Wasserburg (T-W) plots in Figure 11. In general, cassiterite has U concentrations between 2
641 and 70 ppm and lower Th concentrations of <0.01 to 2 ppm. All analyses defined linear trends
642 in T-W diagrams, allowing calculation of lower intercept dates, as reported below. Botryoidal
643 cassiterite sample SRG-62-1 (n = 80 spot analyses) yielded a date of 24.10 ± 0.37 Ma (2σ;
644 MSWD = 3.4) and a Y-axis intercept for initial ^{207}Pb/^{206}Pb of 0.866 ± 0.022 (Fig. 11A).
645 Botryoidal cassiterite sample SR-16-KK-14 (n = 80) yielded a date of 23.88 ± 0.30 Ma (2σ;
646 MSWD = 2.1) and a Y-axis intercept for initial ^{207}Pb/^{206}Pb of 0.843 ± 0.017 (Fig. 11B).

Botryoidal cassiterite sample COCA-80-1 (n = 75) yielded a date of 23.47 ± 0.53 Ma (2σ; MSWD = 1.3) and a Y-axis intercept for initial $^{207}Pb/^{206}Pb$ of 0.832 ± 0.012 (Fig. 11C). Notably, the U content of this sample (avg. U = 47 ± 9 ppm) is the highest compared to the other cassiterite samples (avg. U = 19 ± 8 ppm). Coarse-grained cassiterite sample SRG-95 (n = 80) yielded a date of 23.78 ± 0.22 Ma (2σ; MSWD = 2.7) and a Y-axis intercept for initial $^{207}Pb/^{206}Pb$ of 0.835 ± 0.016 (Fig. 11D). In summary, the four cassiterite samples analyzed yielded dates that range from 23.47 to 24.10 Ma, which overlap within their associated uncertainties.

Major and trace element composition of cassiterite

Cassiterite from San Rafael shows a restricted range in compositions with SnO_2 contents between 93.7 and 100 wt.%. Of the other major elements measured, only FeO (0.2-3.9 wt.%), WO_3 (up to 1.5 wt.%), and TiO_2 (up to 0.6 wt.%) are present above the detection limits of the EMPA (Table A4). Minor elements detected by EMPA include Ta_2O_5 (up to 0.09 wt.%), In_2O_3 (up to 0.06 wt.%), Nb_2O_5 (up to 0.05 wt.%), and MnO (up to 0.02 wt.%; Table A4). Botryoidal cassiterite (samples SR-16-KK-14 and SRG-62-1) is characterized by higher FeO (0.2-3.9 wt.%, avg. = 2.3 wt.%) and lower WO_3 (<0.01-0.26 wt.%, avg = 0.08 wt.%) and TiO_2 (<0.01-0.20 wt.%, avg. = 0.01 wt.%) compared to coarse-grained cassiterite (sample SRG-95) which conversely has lower FeO (0.2-2.1 wt.%, avg. = 0.9 wt.%) and higher WO_3 (<0.01-1.5 wt.%, avg. = 0.2 wt.%) and TiO_2 (<0.01-0.56 wt.%, avg. = 0.11 wt.%).

The cassiterite trace element data are reported in Table A5 and illustrated in Figures 12 to 15. Cassiterite generally shows the following features: 1) very low to low contents (<0.1-10 ppm) of Sc, V, Cr, Mn, Cu, Zn, Ga, Ge, As, Y, Zr, Nb, Mo, Ag, Cd, Hf, Ta, Pb, Th, U, and all REEs; 2) intermediate contents (10s to 100 ppm) of Al and In; and 3) high to very high contents (100s to >1,000 ppm) of Ti, Fe, and W. Botryoidal and coarse-grained cassiterites have

overlapping concentrations for most of the trace elements, however they have contrasting regression lines of element correlations, as seen in binary diagrams (Fig. 12). The concentrations of high field strength elements (HFSE) are low, including Zr (0.06-13.8 ppm; avg. = 1.2 ppm), Hf (<0.01-0.91 ppm; avg. = 0.03 ppm), Nb (0.03-137 ppm; avg. = 14.2 ppm), and Ta (<0.01-5.7 ppm; avg. = 0.22 ppm), with highly variable Zr/Hf (4-41; avg. = 18) and Nb/Ta (7-3,474; avg. = 299) ratios. The critical metal contents are also low for Ga (1.1-29.5 ppm; avg. = 17.4 ppm), Ge (0.15-3.1 ppm; avg. = 1.8 ppm), and In (1.3-49.6 ppm; avg. = 29.8 ppm), but are elevated for W (34-10,290 ppm; avg. = 1277 ppm). In multi-element diagram normalized to upper continental crust (UCC), cassiterite shows relative enrichment in In and W, and partly in Nb and Ta, between 1 and 1,000 times higher than the UCC values, and relative depletion in Sc, V, Ti, Mn, Fe, Y, Zr, Hf, and partly Nb and Ta, between 1 and 1,000 times lower than the UCC values (Fig. 13A). The total REE contents of cassiterite are uniformly low (1.3-9.3 ppm; avg. = 2.7 ppm) and show rather parallel patterns with irregular tetrad distribution in chondrite-normalized diagrams (Fig. 13B), marked by negative Ce and Eu anomalies ($(Ce/Ce^*)_N$ = 0.21-0.77, $(Eu/Eu^*)_N$ = 0.14-0.81), and variable ratios of $(La/Yb)_N$ (0.50-4.14), $(La/Sm)_N$ (0.82-1.31), and $(Gd/Yb)_N$ (0.69-6.54). The calculated tetrad T1 (La to Nd) and T3 (Gd to Ho) factors are >0.2 with T1 and T3 values consistently <0.8, implying a significant concave tetrad effect (Monecke et al., 2002).

Geochemical profiles performed across the growth banding in cassiterite, as seen in transmitted light photomicrographs and matched by CL images, show variation of several trace elements along growth direction (Figs. 14 and 15). Concentrations of Fe, W and Ti vary across such growth zones between 1,000 and 10,000 ppm, 50 and 10,000 ppm, and 10 and 1,000 ppm, respectively, and correlate with the color banding and CL contrasts. We further note that the optically brownish bands show blue-greenish luminescence and have higher contents of W and

Nb and lower contents of Ga and In, whereas the yellow-orange bands have a dark luminescence and correlate negatively in their trace element contents.

Discussion

Chronology of magmatic crystallization and cooling of the SRIC

A summary of all geochronological data for the San Rafael Sn (-Cu) deposit is presented in Figure 16. The $^{40}Ar/^{39}Ar$ plateau dates for magmatic biotite phenocrysts from the cordierite-bearing megacrystic granite overlap within uncertainty from 24.10 ± 0.26 Ma to 24.52 ± 0.28 Ma (2σ; Fig. 6). Biotite from the least altered granite sample COCA-1800 shows the highest K content (ca. 7.3 wt.%) among all the biotite separates and thus yielded what is considered the least disturbed of these $^{40}Ar/^{39}Ar$ plateau dates at 24.10 ± 0.26 Ma (Fig. 6D). This date is interpreted as recording the time when biotite cooled below its Ar closure temperature of ca. 300°C (Harrison et al., 1985; Grove and Harrison, 1996). This age overlaps with the LA-ICP-MS U-Pb zircon date of 24.02 ± 0.25 Ma (Harlaux et al., 2021b) determined on a sample of cordierite-biotite megacrystic granite taken from the currently deepest accessible part of the SRIC (level 3,610 masl) and interpreted as the crystallization age of the upper part of the pluton. This sample yielded an average crystallization temperature of ca. 730 ± 50°C based on Ti-in-zircon thermometry (Harlaux et al., 2021b). This age is also in close agreement with the isotope dilution – thermal ionization mass spectrometry (ID-TIMS) $^{206}Pb/^{238}U$ concordant dates for zircon and monazite fractions of 24.70 ± 0.20 Ma and 24.60 ± 0.20 Ma (2σ), respectively, obtained for the cordierite-biotite megacrystic granite (sample COCA-408; level 4,533 masl) in the upper part of the SRIC (Kontak and Clark, 2002; Table A6; Fig. A8).

The slight age discrepancy between the ID-TIMS and LA-ICP-MS zircon ages has been interpreted by Harlaux et al. (2021b) to reflect the possible contribution of older, inherited

zircon and monazite cores, accidentally analyzed by the bulk ID-TIMS measurements. This interpretation is likely because ID-TIMS analysis of large monazite grains from the San Rafael megacrystic granite showed evidence of inheritance with $^{206}Pb/^{238}U$ date as old as 34.30 ± 0.20 Ma (Table A6; Fig. A8). Alternatively, it is also possible that the dated zircon samples, spatially separated by about 1 km vertically, correspond to two distinct batches of granitic magmas which were injected sequentially during the building of the SRIC. That both the U-Pb zircon and $^{40}Ar/^{39}Ar$ biotite ages overlap indicates that the upper part of the SRIC cooled rapidly, suggesting an upper crustal emplacement level of the granitic pluton.

The biotite samples showing slightly disturbed $^{40}Ar/^{39}Ar$ spectra, with apparent dates between 24.50 ± 0.30 Ma and 24.90 ± 0.30 Ma (2σ; Fig. 7) and with associated elevated MSWD values >> 1, are interpreted to reflect ^{37}Ar and/or ^{39}Ar recoil loss and partly radiogenic ^{40}Ar loss (Kelley, 2002; Schaen et al., 2021), possibly related to the various degrees of chloritization (Roberts et al., 2001; Di Vincenzo et al., 2003) observed in these samples (Fig. A5). These samples have up to 0.8 wt.% lower K content compared to sample COCA-1800. This interpretation is supported by previous conventional K/Ar dating of biotite from both the San Rafael and Quenamari granites and regional equivalents that also yielded older dates between 24.90 ± 0.50 Ma and 27.1 ± 1.0 Ma (2σ; Clark et al., 1983; Kontak et al., 1986, 1987).

Two further aspects of the biotite $^{40}Ar/^{39}Ar$ data are explored, albeit noting the possible influence in regard to possible excess Ar in samples affected by alteration. Firstly, the average biotite ages for the megacrystic granites at San Rafael (n = 5) and Quenamari (n = 3) are 24.30 ± 0.50 Ma (2σ) and 24.40 ± 0.30 Ma (2σ), respectively. The fact that these data overlap within uncertainty the $^{40}Ar/^{39}Ar$ age of the San Rafael COCA-1800 biotite sample and also the ID-TIMS U-Pb zircon data suggests that, overall, the effect of alteration on the Ar systematics in biotite was negligible. Furthermore, the fact that the average dates of the two intrusive centers are the same within uncertainty is consistent with both geological and petrological constraints

(Kontak and Clark, 2002; Harlaux et al., 2021b). Secondly, the accuracy of the biotite $^{40}Ar/^{39}Ar$ ages can be directly assessed by comparison with the results for the three biotite samples previously dated using the Rb/Sr method (Kontak et al., 1987). These ages, recalculated using the newly defined decay constant of $\lambda^{87}Rb = 1.397 \times 10^{-11}$ a^{-1} (Villa et al., 2015) and using a value of $^{87}Sr/^{86}Sr_{(i)} = 0.718$ (Kontak et al., 1987), are the following (inverse isochron ages in parentheses): COCA-151 = 23.70 Ma (24.50 Ma), COCA-194 = 24.00 Ma (24.30 Ma), and COCA-197 = 24.10 Ma (24.70 Ma). The associated uncertainties for the model Rb/Sr ages are estimated at ± 0.50 Ma. Thus, for these three biotite samples, there is a good agreement between the $^{40}Ar/^{39}Ar$ and Rb/Sr chronometers, but we do note that the $^{40}Ar/^{39}Ar$ dates are consistently older by between 0.30 and 0.70 Ma which is, as noted, attributed to the effect of chlorite alteration and related recoil.

The K-feldspar phenocrysts from the main cordierite-biotite megacrystic granite all show U-shaped argon release spectra typical of excess ^{40}Ar, which likely records a fluid-rich open-system (Kelley, 2002) and has been reported to be present as fluid inclusions in K-feldspar by previous studies (e.g., Burgess et al., 1992). This interpretation is consistent with the presence of variable amounts of perthite (i.e., film, flame, and bleb), secondary fluid inclusions, and micro-pores in the K-feldspars in most samples studied from the SRIC, in addition to the local development of late-stage adularia veinlets in K-feldspar phenocrysts, which all indicate variable degrees of interaction with hydrothermal fluids (Kontak et al., 1984; Kontak and Clark, 2002; Fig. A6). For three of the four samples analyzed, the $^{40}Ar/^{39}Ar$ apparent dates calculated for the high-temperature steps for these spectra are centered around 24.20 Ma (Fig. 8), which is similar to the $^{40}Ar/^{39}Ar$ cooling dates of magmatic biotite and overlapping with that of sample COCA-1800. In contrast, the $^{40}Ar/^{39}Ar$ apparent dates calculated for the low-temperature steps are slightly variable, ranging between 22.50 ± 0.40 Ma and 23.70 ± 0.40 Ma (2σ; Fig. 8). These two domains in K-feldspar are interpreted below in regard to San Rafael samples COCA-165B,

771 COCA-190, and COCA-198, and follow on earlier studies of K-feldspar in the SRIC referred
772 to previously.

773 The fact that the development of different structural, textural, and compositional
774 domains in K-feldspar is relevant to K/Ar, and by extension to $^{40}Ar/^{39}Ar$ dating, has long been
775 known (e.g., Dalrymple and Lanphere, 1969). This relationship has thus provided the means to
776 model age spectra obtained from K-feldspar as relating to variable Ar diffusion and thus
777 assesses the thermal evolution of studied samples. This approach has not however been without
778 controversy, as discussed for example by Parsons et al. (1999) and Harrison et al. (2010).
779 Important to the present study is the general recognition that different structural domains in K-
780 feldspar make them susceptible to variable resetting with disordered parts more likely to retain
781 Ar and the coarser perthitic textured and more Or-enriched parts more likely to be reset, in
782 particular where this is fluid assisted (Harrison et al., 2010 and references therein).

783 In this context, therefore, we interpret the results of the $^{40}Ar/^{39}Ar$ dating of K-feldspar
784 (Fig. 8) to indicate the following: 1) the older domains dated at ca. 24.20 Ma equate to the less
785 unmixed and disordered (i.e., with higher Or compositions and dominated by cryptoperthite
786 and film perthite) phases; and 2) the younger domains dated at <23.20 Ma represent areas that,
787 as noted above, are characterized by having higher Or contents (i.e., record a lower temperature
788 equilibration), more perthite, a more ordered structure, and both abundant pitting (i.e.,
789 decrepitated fluid inclusions) and inundated with preserved fluid inclusions. We suggest that
790 these latter features of K-feldspar, although formed earlier in the paragenesis during cooling of
791 the granite, essentially controlled later diffusion and/or fluid-mediated loss of Ar (Parsons et
792 al., 1988, 1999). Also significant is the noted presence of adularia veinlets in some K-feldspars
793 (Fig. A6), which possibly equate paragenetically with the formation of the stage IV adularia as
794 discussed below.
795

Timing of hydrothermal alteration and Sn (-Cu) mineralization

Greisenization of the granitic cupola occurred between 24.18 ± 0.24 Ma and 24.36 ± 0.24 Ma (2σ; Fig. 9) based on the $^{40}Ar/^{39}Ar$ plateau dates for hydrothermal muscovite, which are interpreted to record the Ar closure temperature of muscovite (ca. 400°C; Harrison et al., 2009). The resulting average $^{40}Ar/^{39}Ar$ age of 24.24 ± 0.24 Ma (2σ) is consistent within uncertainty with the previous K/Ar age of 23.60 ± 0.60 Ma (2σ), determined on the muscovite sample COCA-247 (Kontak et al., 1987). Furthermore, it indicates that the early greisen alteration, which is restricted to the upper part of the SRIC, was coeval with cooling of the parental intrusion. The fact that the quartz in sample COCA-247 is inundated with both monophase vapor and vapor-rich fluid inclusions with lesser halite-bearing fluid inclusion types, as discussed by Kontak and Clark (2002), reflects phase separation and thus also indicates a high-level of granite emplacement (i.e., <615 bars or <2.3 km).

The greisen development is interpreted to be contemporaneous with the emplacement of quartz-tourmaline veins and breccias of pre-ore stage I, as shown by our new observations and previous descriptions (Kontak and Clark, 2002; Gialli et al., 2019; Harlaux et al., 2021b). The formation of the well-developed quartz-tourmaline veins and breccias, and variable abundances of both coarse radial tourmaline in K-feldspar and disseminated tourmaline in the granitic groundmass, possibly reflects a pulsing magmatic-hydrothermal system that could have been triggered by the injection of a B-rich silicate melt into a long-lived underlying magmatic reservoir (Harlaux et al., 2020). This interpretation is corroborated by the occurrence of a tourmaline-bearing leucogranite plug in the northwestern part of the San Rafael granite having a more evolved geochemical composition and interpreted as a later B-rich intrusive phase of the SRIC (Kontak and Clark, 2002; Harlaux et al., 2021b).

All four dated cassiterite samples represent the main ore stage II, the most important, but not the sole Sn depositional episode at San Rafael. These U-Pb cassiterite dates all overlap

821 within uncertainty between 23.47 ± 0.53 Ma and 24.10 ± 0.37 Ma (2σ; Fig. 11). These are
822 interpreted as crystallization ages owing to the elevated closure temperature for Pb diffusion in
823 cassiterite (>600°C; Zhang et al., 2011). Importantly, the latter temperature is well above the
824 inferred crystallization temperature of ca. 350-400°C estimated for San Rafael cassiterite from
825 previous fluid inclusion and mineral chemical studies (Palma, 1981; Kontak and Clark, 2002;
826 Wagner et al., 2009; Prado Flores, 2015). This indicates that deposition of large amounts of
827 cassiterite during the main ore stage II occurred during a short-lived hydrothermal pulse of <1
828 Myr duration after the emplacement and cooling of the SRIC and shortly after formation of the
829 stage I quartz-tourmaline veins and breccias. Given the upper crustal emplacement level of the
830 SRIC and the need to sustain temperatures of mineralization up to 350-400°C, the duration of
831 stage II was likely on the order of <0.5 Myr, as has been demonstrated for short-lived
832 mineralizing episodes in porphyry-type magmatic-hydrothermal systems (e.g., Chiaradia et al.,
833 2013; Catchpole et al., 2015; Tapster et al., 2016; Li et al., 2017; Rottier et al., 2020; Large et
834 al., 2021).

835 The fact that the U-Pb cassiterite ages overlap within uncertainty with the $^{40}Ar/^{39}Ar$
836 plateau age of 23.81 ± 0.23 Ma obtained on sanidine from the pristine Antauta cordierite-biotite
837 granitic dike located <12 km south of San Rafael (Kontak et al., 1986; Sandeman et al., 1997)
838 possibly indicates a protracted magmatic activity until the main ore stage II. The precipitation
839 of large amounts of cassiterite in the richly mineralized Sn lodes is interpreted as the result of
840 mixing of Sn-rich magmatic brines exsolved from the underlying magma chamber with
841 modified meteoric water, as supported by previous fluid inclusion, stable isotope, and mineral
842 chemical studies (Kontak and Clark, 2002; Mlynarczyk and Williams-Jones, 2006; Wagner et
843 al., 2009; Harlaux et al., 2020, 2021c; Cazorla Martínez, 2022). That the U-Pb ages for
844 botryoidal and coarse-grained cassiterite cannot be unequivocally resolved within uncertainty

corroborates the petrographic observations showing alternate layers of these two morphological types of cassiterite (Mlynarczyk et al., 2003; Wagner et al., 2009).

The $^{40}Ar/^{39}Ar$ data obtained on adularia from stages III and IV yielded within uncertainty identical plateau dates between 22.72 ± 0.11 Ma and 22.29 ± 0.24 Ma (2σ; Fig. 10), which are consistent with a previous K/Ar age of 22.60 ± 0.50 Ma (2σ) on adularia intergrown with base-metal sulfides of stage III (Clark et al., 1983). The new adularia dates are interpreted as crystallization ages and thus record cooling of the hydrothermal system below the Ar closure temperature of orthoclase (ca. 300-350°C; Cassata and Renne, 2013). This indicates that the quartz-carbonate-adularia±fluorite veins of stage IV, partly overlapping with the polymetallic (Cu-Zn-Pb-Ag-Sn) mineralization of stage III, record the youngest dated hydrothermal stage in the San Rafael deposit. Therefore, the geochronological data demonstrate that this late hydrothermal event in the lifespan of the magmatic-hydrothermal system postdated by ca. 1 Myr the deposition of the main Sn ore stage. As we already noted, the spread of the younger $^{40}Ar/^{39}Ar$ age spectra between ca. 23.70 and 22.50 Ma for K-feldspar phenocrysts (Fig. 8) is interpreted to record successive pulses of hydrothermal fluids between stages II and IV, including introduction of additional Sn during stage III.

To summarize, the San Rafael magmatic-hydrothermal system was active for an overall period of at least 2 Myr, from late Oligocene to early Miocene, following initial emplacement of the earliest granitic phase of the SRIC. The lifetime of the magmatic-hydrothermal system was likely sustained by protracted magmatic activity in the underlying reservoir (i.e., magma recharge) resulting in cyclic release of magmatic-hydrothermal pulses. The latest polymetallic stages postdating the main Sn ore stage by ca. 1 Myr reflect the waning of the hydrothermal system accompanied by additional incursion of meteoric groundwaters.

Trace elements in San Rafael cassiterite and comparison with the Bolivian tin belt

Trace element compositions of cassiterite from San Rafael are similar to the ones of other Oligocene-Miocene Sn deposits in the Bolivian tin belt (Fig. 13A; Gemmrich et al., 2021). Cassiterite is notably depleted in Nb, Ta, In, Ge, and Ga whose contents are comparable to those of cassiterite from the Bolivian Sn deposits (Gemmrich et al., 2021). The highly variable Zr/Hf (4-41) and Y/Ho (2-27) ratios in cassiterite fall outside of the CHArge-and-RAdius-Controlled (CHARAC) field as defined by Bau (1996). This indicates trace element fractionation caused by different complex formation in aqueous solutions, as also shown for other hydrothermal oxides (e.g., Harlaux et al., 2018b; Schirra and Laurent, 2021). Similarly, the Nb/Ta ratio (7-3474) in cassiterite is extremely variable, which could result from fluid mixing, variable degrees of fluid-rock interaction, or chemical disequilibrium at the mineral/fluid interface (Lerouge et al., 2017; Cheng et al., 2019; Bennett et al., 2020). The strong positive correlation between V and Sc observed in San Rafael cassiterite (Fig. 12G) supports the heterovalent coupled substitution $Sc^{3+} + V^{5+} = 2Sn^{4+}$ proposed by previous studies (Cheng et al., 2019; Gemmrich et al., 2021). Additionally, a clear positive correlation is found between Fe and Ga (Fig. 12B), possibly reflecting the heterovalent substitution $R^{3+} + (Nb,Ta)^{5+} = 2Sn^{4+}$ where $R^{3+} = Fe^{3+}$, Ga^{3+} (Izoret et al., 1985; Tindle and Breaks, 1998).

One of the most characteristic features of the Sn mineralization at San Rafael is the occurrence of large amounts of botryoidal cassiterite ("wood tin"), which is restricted to the stage II of the paragenetic sequence of the deposit. Botryoidal cassiterite has been mainly described in Mexican-type rhyolite-hosted Sn deposits in New Mexico, Nevada, Alaska, Mexico, Bolivia, Russia, Tasmania, and Malaysia (Taylor, 1979; Hutchison, 1988). The conditions required for the formation of "wood tin" are uncertain and previous work proposed several explanations, including supergene oxidation from stannite, crystallization from Sn-rich colloidal silica gels, low temperature (<150°C) encrustations/infillings, or rapid nucleation from supersaturated solutions (e.g., Lufkin, 1977; Taylor, 1979; Hosking et al., 1987).

Interestingly, the trace element compositions of botryoidal and coarse-grained cassiterite from San Rafael are similar, differing only by variable slopes of element correlations in binary diagrams (Fig. 12), such as Fe vs In, Ge vs Ga, or Ti vs Nb. These variable element ratios may indicate contrasting compositions of the Sn-precipitating fluids during deposition of botryoidal and coarse-grained cassiterite, or variable degrees of local fluid-rock interactions. The trace element profiles performed in cassiterite reveal fluctuating concentrations of one to three orders of magnitude for Sc, Ti, V, Fe, Ga, Nb, In, W, and U along the crystal growth direction (Figs. 14-15). Such variations suggest evolving physicochemical fluid conditions in the hydrothermal system over time, possibly caused by repeated mixing of Sn-bearing magmatic brines with meteoric waters and/or fluid chemical disequilibrium induced by rapid nucleation and crystal growth.

The REE spectra of San Rafael cassiterite are characterized by concave tetrad effects and negative Ce and Eu anomalies similar to cassiterite from the Bolivian tin belt (Fig. 13B; Gemmrich et al., 2021). Highly irregular chondrite-normalized REE patterns in hydrothermal minerals combining concave and convex tetrads have been linked to fluid immiscibility and REE liquid-vapor fractionation (e.g., Monecke et al., 2011). In particular, the development of negative Eu anomalies and concave tetrads in hydrothermal minerals is attributed to precipitation from F-rich vapors that separated from a single-phase magmatic fluid (Monecke et al., 2011). Although evidence of boiling was demonstrated during the early, pre-ore evolution of the San Rafael magmatic-hydrothermal system, the precipitation of cassiterite resulted essentially from the mixing between Sn-rich magmatic brines and modified meteoric waters (Kontak and Clark, 2002; Mlynarczyk et al., 2003; Wagner et al., 2009; Harlaux et al., 2020, 2021c).

Experimental and empirical studies of hydrothermal systems indicate that REE-Cl complexes partition readily into brines relative to vapors and that HREE are preferentially

fractionated over LREE into the vapor phase (Shmulovich et al., 2002; Möller et al., 2003, 2009). Accordingly, the Sn-rich magmatic brines acting as the main mineralizing fluid at San Rafael should be enriched in LREE relative to HREE resulting in precipitation of LREE-rich cassiterite. This fractionation is not observed in botryoidal and coarse-grained cassiterite which show similar $(La/Yb)_N$ ratios (0.50-4.14) and uniformly low total REE contents (1.3-9.3 ppm). This inconsistency suggests a crystallographic control on REE incorporation in cassiterite as also described in other minerals like wolframite (Xiong et al., 2017; Harlaux et al., 2018b; Zhang et al., 2018). Indeed, the ionic radii of REE (La^{3+} = 1.03 Å; Lu^{3+} = 0.86 Å) are much larger than that of Sn^{4+} (0.69 Å) in octahedral coordination (Shannon, 1976), suggesting that REE incorporation into cassiterite is crystallographically limited. Another explanation may be the co-crystallization of REE-bearing hydrothermal minerals (e.g., chlorite, monazite, apatite) resulting in low REE contents in cassiterite.

The pronounced negative Ce and Eu anomalies also indicate that these two elements are not easily incorporated into cassiterite due to their large ionic radii and the prevalent stability of Eu^{2+} (1.17 Å) and Ce^{3+} (1.01 Å) over Eu^{3+} (0.95 Å) and Ce^{4+} (0.87 Å), respectively, in hydrothermal fluids (Migdisov et al., 2016; Liu et al., 2017). Furthermore, experimental work demonstrated that the LREEs are more stable and, thus, more mobile than the HREEs in chloride-bearing aqueous solutions and that this difference in stability increases with increasing temperature (Migdisov et al., 2016). Another work showed that the REE contents and the LREE/HREE ratios of cassiterite are strongly influenced by the associated mineral assemblage, the fluid chemistry, and the composition of the host rocks (Plimer et al., 1991). Consequently, the REE composition of cassiterite likely reflects the combination of these different variables and, therefore, is difficult to interpret regarding the geologic process occurring during Sn deposition.

Conclusions

This study demonstrates that the world-class San Rafael Sn (-Cu) deposit formed in a protracted geological period of at least 2 Myr, from late Oligocene to early Miocene, including the following sequence of major events:

(1) Crystallization of the medium- to coarse-grained biotite-cordierite granitic pluton by ca. 24.50 Ma which intruded into host Ordovician metasedimentary rocks. The least disturbed biotite sample from the megacrystic monzogranite yielded an $^{40}Ar/^{39}Ar$ plateau date of 24.10 ± 0.26 Ma, which constrains the time of cooling of the upper part of the stock to <300°C, i.e., the Ar closure temperature of this phase. Such a rapid cooling is consistent with the petrographic features of the granitic stock (e.g., porphyritic dikes with quenched textures, granophyre/graphic intergrowths) and the Al/Si ordering of the K-feldspar megacrysts, which collectively indicate a shallow crustal emplacement (~2-3 km paleodepth).

(2) Localized greisenization in the granite cupola, which was coeval with the cooling of the parental intrusion, occurred at 24.24 ± 0.24 Ma, based on muscovite average $^{40}Ar/^{39}Ar$ plateau ages. This event was contemporaneous with emplacement of quartz-tourmaline veins and breccias of pre-ore stage I. The fact that minor amounts of tourmaline are present in the greisen provides a genetic link to the subsequent onset of alteration and mineralization. Tourmalinization possibly resulted from a pulsing magmatic-hydrothermal system caused by the injection of B-rich silicate melt into the underlying crystal mush reservoir.

(3) Deposition of Sn during stage II, the main ore stage, is constrained by LA-ICP-MS U-Pb dating of cassiterite between 24.10 ± 0.37 Ma and 23.47 ± 0.53 Ma. This reflects successive hydrothermal pulses that occurred <1 Myr after the crystallization of the main granitic phases of the SRIC and shortly after emplacement of stage I quartz-tourmaline veins and breccias. The duration of this event is poorly constrained by the associated uncertainties but given the upper

crustal emplacement level and the need to sustain fluid temperatures of up to 350-400°C, its duration was likely on the order of <0.5 Myr.

(4) Formation of the polymetallic sulfide mineralization of stage III and the late quartz-carbonate-fluorite stage IV is constrained by $^{40}Ar/^{39}Ar$ dating of adularia between 22.72 ± 0.11 Ma and 22.29 ± 0.24 Ma. This timing is further supported by the U-shaped $^{40}Ar/^{39}Ar$ spectra for K-feldspar phenocrysts from the cordierite-biotite megacrystic granite and their partial resetting which have minima ages at ca. 22.50 Ma. These age spectra are typical of excess Ar in a fluid-rich open system and are in agreement with hydrothermal circulations during stages II to IV, including introduction of additional Sn during stage III. The geochronological data indicate therefore that the magmatic-hydrothermal system remained active for ca. 1 Myr following the main Sn ore stage, resulting in polymetallic sulfide mineralization.

This study provides further evidence that the present-day exposed level of the San Rafael granite was a passive host for the Sn mineralization and only provided the structural focusing for mineralizing fluids derived from a deeper part of the magmatic system. Botryoidal and coarse-grained cassiterite from stage II are characterized by similar trace element compositions with fluctuating metal contents across growth banding. These variations suggest significant changes of physicochemical conditions of the hydrothermal system during cassiterite precipitation, likely caused by rapid and repeated mixing between magmatic fluids and meteoric groundwaters.

Acknowledgments

This research was supported by a Swiss National Science Foundation grant (S19053_169901) to Lluís Fontboté, the company Minsur S.A, and by Natural Sciences and Engineering Research Council of Canada grants to Alan H. Clark and Edward Farrar. Logistic support in the field was

provided by the geologist teams from Minsur S.A., who are gratefully acknowledged here. This contribution is dedicated to the memory of Edward Farrar, pioneering geochronologist, who for over forty years provided the temporal framework essential to the Queen's University Central Andean Metallogenetic Project. The authors are also grateful to Douglas A. Archibald, Yanshao Chen, Hamish A. Sandeman, and Hardolph A. Wasteneys for providing technical support with acquisition of the geochronological data. This paper benefited from the critical comments of Jay Thompson on an earlier version of the manuscript. Finally, we would like to thank three anonymous reviewers, as well as the Associate Editor Massimo Chiaradia and the Editor-in-Chief Larry Meinert for their constructive comments, which helped to improve the original manuscript.

References

Arenas, M.J., 1980, El distrito minero San Rafael: Estaño en el Perú: Boletín de la Sociedad Geológica del Perú, v. 66, p. 1–11.

Baksi, A.K., Archibald, D.A., and Farrar, E., 1996, Intercalibration of $^{40}Ar/^{39}Ar$ dating standards: Chemical Geology, v. 129, p. 307-324.

Bau, M., 1996, Controls on the fractionation of isovalent trace elements in magmatic and aqueous systems: evidence from Y/Ho, Zr/Hf, and lanthanide tetrad effect: Contributions to Mineralogy and Petrology, v. 123, p. 323–333.

Benites, D., Torró, L., Vallance, J., Laurent, O., Quispe, P., Rosas, S., Uzieda, M.F., Holm-Denoma, C.S., Pianowski, L.S., Camprubí, A., Colás, V., Fernández-Baca, A., Giraldo, L., Chelle-Michou, C., Sáez, J., Kouzmanov, K., and Fontboté, L., 2022, Geology, mineralogy, and cassiterite geochronology of the Ayawilca Zn-Pb-Ag-In-Sn-Cu deposit, Pasco, Peru: Mineralium Deposita, v. 57, p. 481-507.

Bennett, J.M., Kemp, A.I., and Roberts, M.P., 2020, Microstructural controls on the chemical heterogeneity of cassiterite revealed by cathodoluminescence and elemental X-ray mapping: American Mineralogist, v. 105, p. 58-76.

Buret, Y., von Quadt, A., Heinrich, C., Selby, D., Wälle, M., and Peytcheva, I., 2016, From a long-lived upper-crustal magma chamber to rapid porphyry copper emplacement: Reading the geochemistry of zircon crystals at Bajo de la Alumbrera (NW Argentina): Earth and Planetary Science Letters, v. 450, p. 120-131.

Burgess, R., Kelley, S.P., Parsons, I., Walker, F.D.L., and Worden, R.H., 1992, $^{40}Ar/^{39}Ar$ analysis of perthite microtextures and fluid inclusions in alkali feldspars from the Klokken syenite, South Greenland: Earth and Planetary Science Letters, v. 109, p. 147-167.

Carr, P.A., Zink, S., Bennett, V.C., Norman, M.D., Amelin, Y., and Blevin, P.L., 2020, A new method for U-Pb geochronology of cassiterite by ID-TIMS applied to the Mole Granite polymetallic system, eastern Australia: Chemical Geology, v. 539, p. 119539.

Carr, P.A., Mercadier, J., Harlaux, M., Romer, R.L., Moreira, E., Legros, H., Cuney, M., Marignac, M., Cauzid, J., Salsi, L., Lecomte, A., Rouer, O., and Peiffert, C., 2021, U/Pb geochronology of wolframite by LA-ICP-MS; mineralogical constraints, analytical procedures, data interpretation, and comparison with ID-TIMS: Chemical Geology, v. 584, p. 120511.

Cassata, W.S., and Renne, P.R., 2013, Systematic variations of argon diffusion in feldspars and implications for thermochronometry: Geochimica et Cosmochimica Acta, v. 112, p. 251-287.

Catchpole, H., Kouzmanov, K., Bendezú, A., Ovtcharova, M., Spikings, R., Stein, H., and Fontboté, L., 2015, Timing of porphyry (Cu-Mo) and base metal (Zn-Pb-Ag-Cu) mineralisation in a magmatic-hydrothermal system—Morococha district, Peru: Mineralium Deposita, v. 50, p. 895-922.

Cazorla Martínez, M., 2022, Fluid evolution in the San Rafael Sn-Cu lode deposit, Peru: Unpublished M.Sc. thesis, University of Geneva, Switzerland, 119 p.

Cernuschi, F., Dilles, J.H., Grocke, S.B., Valley, J.W., Kitajima, K., and Tepley III, F.J., 2018, Rapid formation of porphyry copper deposits evidenced by diffusion of oxygen and titanium in quartz: Geology, v. 46, p. 611-614.

Chelle-Michou, C., Chiaradia, M., Selby, D., Ovtcharova, M., and Spikings, R.A., 2015, High-resolution geochronology of the Coroccohuayco porphyry-skarn deposit, Peru: A rapid product of the Incaic Orogeny: Economic Geology, v. 110, p. 423-443.

Chen, L.L., Ni, P., Dai, B.Z., Li, W.S., Chi, Z., and Pan, J.Y., 2019, The genetic association between quartz vein-and greisen-type mineralization at the Maoping W–Sn deposit,

southern Jiangxi, China: insights from zircon and cassiterite U–Pb ages and cassiterite trace element composition: Minerals, v. 9, p. 411.

Cheng, Y., Spandler, C., Kemp, A., Mao, J., Rusk, B., Hu, Y., and Blake, K., 2019, Controls on cassiterite (SnO_2) crystallization: Evidence from cathodoluminescence, trace-element chemistry, and geochronology at the Gejiu Tin District: American Mineralogist, v. 104, p. 118-129.

Chiaradia, M., Schaltegger, U., Spikings, R., Wotzlaw, J.F., and Ovtcharova, M., 2013, How accurately can we date the duration of magmatic-hydrothermal events in porphyry systems? - An invited paper: Economic Geology, v. 108, p. 565-584.

Clark, A.H., Palma, V.V., Archibald, D.A., Farrar, E., Arenas F.M.J., and Robertson, R.C., 1983, Occurrence and age of tin mineralization in the Cordillera Oriental, southern Peru: Economic Geology, v. 78, p. 514-520.

Clark, A.H., Farrar, E., Kontak, D.J., Langridge, R.J., Arenas F.M.J., France, L.J., McBride, S.L., Woodman, P.L., Wasteneys, H.A., Sandeman, H.A., and Archibald, D.A., 1990, Geologic and geochronologic constraints on the metallogenic evolution of the Andes of southeastern Peru: Economic Geology, v. 85, p. 1520-1583.

Corthay, G., 2014, The Quenamari prospect, San Rafael tin district, southern Peru: Geology, mineral assemblages, fluid inclusion microthermometry, and stable isotopes: Unpublished M.Sc. thesis, University of Geneva, Switzerland, 113 p.

Dalrymple, G.B., and Lanphere, M.A., 1969, Potassium-argon dating: Principles, techniques and applications to geochronology, 258 p.

Deckart, K., Clark, A.H., Celso, A.A., Ricardo, V.R., Bertens, A.N., Mortensen, J.K., and Fanning, M., 2005, Magmatic and hydrothermal chronology of the giant Río Blanco porphyry copper deposit, central Chile: Implications of an integrated U-Pb and $^{40}Ar/^{39}Ar$ database: Economic Geology, v. 100, p. 905-934.

1079 Denholm, J.L., Stepanov, A.S., Meffre, S., Bottrill, R.S., and Thompson, J.M., 2021, The
1080 Geochronology of Tasmanian Tin Deposits Using LA-ICP-MS U-Pb Cassiterite Dating:
1081 Economic Geology, v. 116, p. 1387-1407.
1082 Di Vincenzo, G., Viti, C., and Rocchi, S., 2003, The effect of chlorite interlayering on ^{40}Ar–
1083 ^{39}Ar biotite dating: an ^{40}Ar–^{39}Ar laser-probe and TEM investigations of variably chloritised
1084 biotites: Contributions to Mineralogy and Petrology, v. 145, p. 643-658.
1085 Einaudi, M.T., Hedenquist, J.W., and Inan, E.E., 2003, Sulfidation state of fluids in active and
1086 extinct hydrothermal systems: Transitions from porphyry to epithermal environments:
1087 Society of Economic Geologists, Special Publication 10, p. 285–313.
1088 Gemmrich, L., Torró, L., Melgarejo, J.C., Laurent, O., Vallance, J., Chelle-Michou, C., and
1089 Sempere, T.P., 2021, Trace element composition and U-Pb ages of cassiterite from the
1090 Bolivian tin belt: Mineralium Deposita, v. 56, p. 1491-1520.
1091 Gialli, S., Chauvet, A., Kouzmanov, K., Dini, A., Spikings, R., Kalinaj, M., and Fontboté, L.,
1092 2017, Structural control of the world-class Sn district of San Rafael, Peru: Society of
1093 Economic Geologists (SEG) 2017: Ore Deposits of China and Beyond, Beijing, China,
1094 September 17–20, 2017, Proceedings, p. 206.
1095 Gialli, S., Harlaux, M., Kouzmanov, K., Fontboté, L., Chauvet, A., Laurent, O., Dini, A., and
1096 Kalinaj, M., 2019, Early hydrothermal alteration stages at the giant San Rafael tin deposit,
1097 Peru: Proceedings of the 15th SGA Biennial Meeting, 27-30 August 2019, Glasgow,
1098 Scotland, v. 1, p. 361–364.
1099 Grant, J.N., Halls, C., Avila Salinas, W., and Snelling, N.J., 1979, K-Ar ages of igneous rocks
1100 and mineralization in part of the Bolivian tin belt: Economic Geology, v. 74, p. 838-851.
1101 Grant, J.N., Halls, C., Sheppard, S.M.F., and Avila, W., 1980, Evolution of the Porphyry Tin
1102 Deposits of Bolivia: Mining Geology Special Issue, v. 8, p. 151-173.

1103 Grove, M., and Harrison, T.M., 1996, ^{40}Ar* diffusion in Fe-rich biotite: American Mineralogist,
1104 v. 81, p. 940–951.
1105 Guillong, M., Hametner, K., Reusser, E., Wilson, S.A., and Günther, D., 2005, Preliminary
1106 characterisation of new glass reference materials (GSA-1G, GSC-1G, GSD-1G and GSE-
1107 1G) by laser ablation-inductively coupled plasma-mass spectrometry using 193 nm, 213
1108 nm and 266 nm wavelengths: Geostandards and Geoanalytical Research, v. 29, p. 315-331.
1109 Guillong, M., Meier, D.L., Allan, M.M., Heinrich, C.A., and Yardley, B.W.D., 2008, SILLS:
1110 A MATLAB-based program for the reduction of laser ablation ICP-MS data of
1111 homogeneous materials and inclusion, in Sylvester, P., ed., Laser Ablation ICP-MS in the
1112 Earth Sciences: Current practices and outstanding issues: Mineralogical Association of
1113 Canada Short Course Series, v. 40, p. 328–333.
1114 Harlaux, M., Romer, R.L., Mercadier, J., Morlot, C., Marignac, C., and Cuney, M., 2018a, 40
1115 Ma of hydrothermal W mineralization during the Variscan orogenic evolution of the
1116 French Massif Central revealed by U-Pb dating of wolframite: Mineralium Deposita, v. 53,
1117 p. 21-51.
1118 Harlaux, M., Mercadier, J., Marignac, C., Peiffert, C., Cloquet, C., and Cuney, M., 2018b,
1119 Tracing metal sources in peribatholitic hydrothermal W deposits based on the chemical
1120 composition of wolframite: The example of the Variscan French Massif Central: Chemical
1121 Geology, v. 479, p. 58-85.
1122 Harlaux, M., Kouzmanov, K., Gialli, S., Laurent, O., Rielli, A., Dini, A., Chauvet, A., Menzies,
1123 A., Kalinaj, M., and Fontboté, L., 2020, Tourmaline as a Tracer of Late-Magmatic to
1124 Hydrothermal Fluid Evolution: The World-Class San Rafael Tin (-Copper) Deposit, Peru:
1125 Economic Geology, v. 115, p. 1665–1697.
1126 Harlaux, M., Marignac, C., Mercadier, J., Poujol, M., Boiron, M.C., Kouzmanov, K., Camacho,
1127 A., Alikouss, S., Roméo, B., Mouthier, B., and Cuney, M., 2021a, Multistage development

of a hydrothermal W deposit during the Variscan late-orogenic evolution: the Puy-les-Vignes breccia pipe (Massif Central, France): BSGF-Earth Sciences Bulletin, v. 192, p. 33.

Harlaux, M., Kouzmanov, K., Gialli, S., Clark, A.H., Laurent, O., Corthay, G., Prado Flores, E., Dini, A., Chauvet, A., Ulianov, A., Chiaradia, M., Menzies, A., Villón Durand, G., Kalinaj, M., and Fontboté, L., 2021b, The upper Oligocene San Rafael intrusive complex (Eastern Cordillera, southeast Peru), host of the largest-known high-grade tin deposit: Lithos, v. 400-401, p. 106409.

Harlaux, M., Kouzmanov, K., Gialli, S., Marger, K., Bouvier, A.S., Baumgartner, L.P., Rielli, A., Dini, A., Chauvet, A., Kalinaj, M., and Fontboté, L., 2021c, Fluid mixing as primary trigger for cassiterite deposition: Evidence from in situ $\delta^{18}O$-$\delta^{11}B$ analysis of tourmaline from the world-class San Rafael tin (-copper) deposit, Peru: Earth and Planetary Science Letters, v. 563, p. 116889.

Harrison, T.M., Duncan, I.A.N., and Mcdougall, I.A.N., 1985, Diffusion of ^{40}Ar in biotite: temperature, pressure and compositional effects: Geochimica et Cosmochimica Acta, v. 49, p. 2461-2468.

Harrison, T.M., Célérier, J., Aikman, A.B., Hermann, J., and Heizler, M.T., 2009, Diffusion of ^{40}Ar in muscovite: Geochimica et Cosmochimica Acta, v. 73, p. 1039-1051.

Harrison, T.M., Heizler, M.T., McKeegan, K.D., and Schmitt, A.K., 2010, In situ ^{40}K–^{40}Ca 'double-plus' SIMS dating resolves Klokken feldspar ^{40}K–^{40}Ar paradox: Earth and Planetary Science Letters, v. 299, p. 426-433.

Hosking, K.F.G., Stanley, G.J., and Camm, G.S., 1987, The occurrence, nature and genesis of wood tin in south-west England: Transactions of the Royal Geological Society of Cornwall, v. 21, p. 153-212.

Hu, Z., Gao, S., Liu, Y., Hu, S., Chen, H., and Yuan, H., 2008, Signal enhancement in laser ablation ICP-MS by addition of nitrogen in the central channel gas: Journal of Analytical Atomic Spectrometry, v. 23, p. 1093–1101.

Hu, R.Z., Wei, W.F., Bi, X.W., Peng, J.T., Qi, Y.Q., Wu, L.Y., and Chen, Y.W., 2012, Molybdenite Re–Os and muscovite $^{40}Ar/^{39}Ar$ dating of the Xihuashan tungsten deposit, central Nanling district, South China: Lithos, v. 150, p. 111-118.

Hutchison, C.S., 1988, Geology of Tin Deposits in Asia and the Pacific. Springer, Berlin, Heidelberg, 718 p.

Izoret, L., Marnier, G., and Dusausoy, Y., 1985, Caractérisation cristallochimique de la cassitérite des gisements d'étain et de tungstène de Galice, Espagne: The Canadian Mineralogist, v. 23, p. 221-231.

Jochum, K.P., Weis, U., Stoll, B., Kuzmin, D., Yang, Q., Raczek, I., Jacob, D.E., Stracke, A., Birbaum, K., Frick, D.A., Günther, D., and Enzweiler, J., 2011, Determination of reference values for NIST SRM 610-617 glasses following ISO guidelines: Geostandards and Geoanalytical Research, v. 35, p. 397–429.

Kelley, S., 2002, Excess argon in K–Ar and Ar–Ar geochronology: Chemical Geology, v. 188, p. 1-22.

Kelly, W.C., and Turneaure, F.S., 1970, Mineralogy, paragenesis and geothermometry of the tin and tungsten deposits of the eastern Andes, Bolivia: Economic Geology, v. 65, p. 609-680.

Kontak, D.J., 1985, The magmatic and metallogenetic evolution of a craton-orogen interface: The Cordillera de Carabaya, central Andes, SE Peru: Unpublished Ph.D. thesis, Kingston, Ontario, Queen’s University, 714 p.

1174 Kontak, D.J., and Clark, A.H., 2002, Genesis of the giant, bonanza San Rafael lode tin deposit,
1175 Peru: Origin and significance of pervasive alteration: Economic Geology, v. 97, p. 1741-
1176 1777.
1177 Kontak, D., Clark, A.H., and Farrar, E., 1984, The influences of fluid and rock compositions,
1178 and tectono-thermal processes on Al-Si distribution in alkali feldspars in granitoid rocks,
1179 S.E. Peru: Bulletin de Minéralogie, v. 107, p. 387-400.
1180 Kontak, D.J., Clark, A.H., Farrar, E., Pearce, T.H., Strong, D.F., and Baadsgaard, H., 1986,
1181 Petrogenesis of a Neogene shoshonite suite, Cerro Moromoroni, Puno, southeastern Peru:
1182 The Canadian Mineralogist, v. 24, p. 117-135.
1183 Kontak, D.J., Clark, A.H., Farrar, E., Archibald, D.A., and Baadsgaard, H., 1987,
1184 Geochronological data for Tertiary granites of the southeast Peru segment of the central
1185 Andean tin belt: Economic Geology, v. 82, p. 1611-1618.
1186 Kontak, D.J., Clark, A.H., Farrar, E., Archibald, D.A., and Baadsgaard, H., 1990a, Late
1187 Paleozoic-early Mesozoic magmatism in the Cordillera de Carabaya, Puno, southeastern
1188 Peru: geochronology and petrochemistry: Journal of South American Earth Sciences, v.
1189 3, p. 213–230.
1190 Kontak, D.J., Cumming, G.L., Krstic, D., Clark, A.H., and Farrar, E., 1990b, Isotopic
1191 composition of lead in ore deposits of the Cordillera Oriental, southeastern Peru:
1192 Economic Geology, v. 85, p. 1584–1603.
1193 Koppers, A.A., 2002, ArArCALC—software for $^{40}Ar/^{39}Ar$ age calculations: Computers and
1194 Geosciences, v. 28, p. 605-619.
1195 Kuiper, K.F., Deino, A., Hilgen, F.J., Krijgsman, W., Renne, R., and Wijbrans, J.R., 2008,
1196 Synchronizing Rock Clocks of Earth History: Science, v. 320, p. 500-504.
1197 Large, S.J., Buret, Y., Wotzlaw, J.F., Karakas, O., Guillong, M., von Quadt, A., and Heinrich,
1198 C.A., 2021, Copper-mineralised porphyries sample the evolution of a large-volume silicic

magma reservoir from rapid assembly to solidification: Earth and Planetary Science Letters, v. 563, p. 116877.

Legros, H., Harlaux, M., Mercadier, J., Romer, R.L., Poujol, M., Camacho, A., Marignac, C., Cuney, M., Wang, R.C., Charles, N., and Lespinasse, M.Y., 2020, The world-class Nanling metallogenic belt (Jiangxi, China): W and Sn deposition at 160 Ma followed by 30 my of hydrothermal metal redistribution: Ore Geology Reviews, v. 117, p. 103302.

Lehmann, B., Ishihara, S., Michel, H., Miller, J., Rapela, C.W., Sanchez, A., Tistl, M., and Winkelmann, L., 1990, The Bolivian tin province and regional tin distribution in the central Andes: A reassessment: Economic Geology, v. 85, p. 1044-1058.

Lerouge, C., Gloaguen, E., Wille, G., and Bailly, L., 2017, Distribution of In and other rare metals in cassiterite and associated minerals in Sn±W ore deposits of the western Variscan Belt: European Journal of Mineralogy, v. 29, p. 739-753.

Li, Y., Selby, D., Condon, D., and Tapster, S., 2017, Cyclic magmatic-hydrothermal evolution in porphyry systems: High-precision U-Pb and Re-Os geochronology constraints on the Tibetan Qulong porphyry Cu-Mo deposit: Economic Geology, v. 112, p. 1419-1440.Liu, W., Etschmann, B., Migdisov, A., Boukhalfa, H., Testemale, D., Müller, H., Hazemann, J.L., and Brugger, J., 2017, Revisiting the hydrothermal geochemistry of europium (II/III) in light of new in-situ XAS spectroscopy results: Chemical Geology, v. 459, p. 61-74.

Lufkin, J.L., 1977, Chemistry and mineralogy of wood-tin, Black Range, New Mexico: American Mineralogist, v. 62, p. 100-106.

McBride, S.L., Robertson, R.C., Clark, A.H., and Farrar, E., 1983, Magmatic and metallogenetic episodes in the northern tin belt, Cordillera Real, Bolivia: Geologische Rundschau, v. 72, p. 685-713.

McDonough, W.F., and Sun, S.S., 1995, The composition of the Earth: Chemical Geology, v. 120, p. 223-253.

Mercer, C.N., Reed, M.H., and Mercer, C.M., 2015, Time scales of porphyry Cu deposit formation: Insights from titanium diffusion in quartz: Economic Geology, v. 110, p. 587-602.

Migdisov, A., Williams-Jones, A.E., Brugger, J., and Caporuscio, F.A., 2016, Hydrothermal transport, deposition, and fractionation of the REE: Experimental data and thermodynamic calculations: Chemical Geology, v. 439, p. 13–42.

Minsur S.A., 2021, Annual Report: March 28, 2022, 71 p., www.minsur.com.

Mlynarczyk, M.S., 2005, Constraints on the Genesis of Lode-Style Tin Mineralization: Evidence from the San Rafael Tin-Copper Deposit. Peru: Unpublished Ph.D. thesis, McGill University, Montreal, Canada, 360 p.

Mlynarczyk, M.S., and Williams-Jones, A.E., 2005, The role of collisional tectonics in the metallogeny of the Central Andean tin belt: Earth and Planetary Science Letters, v. 240, p. 656-667.

Mlynarczyk, M.S., and Williams-Jones, A.E., 2006, Zoned tourmaline associated with cassiterite: implications for fluid evolution and tin mineralization in the San Rafael Sn–Cu deposit, southeastern Peru: The Canadian Mineralogist, v. 44, p. 347-365.

Mlynarczyk, M.S., Sherlock, R.L., and Williams-Jones, A.E., 2003, San Rafael, Peru: Geology and structure of the worlds richest tin lode: Mineralium Deposita, v. 38, p. 555-567.

Mohammadi, N., McFarlane, C.R., Lentz, D.R., and Thorne, K.G., 2020, Timing of magmatic crystallization and Sn–W–Mo greisen vein formation within the Mount Douglas Granite, New Brunswick, Canada: Canadian Journal of Earth Sciences, v. 57, p. 814-839.

Möller, P., Dulski, P., and Morteani, G., 2003, Partitioning of rare earth elements, yttrium, and some major elements among source rocks, liquid and vapor of Larderello-Travale Geothermal Field, Tuscany (Central Italy): Geochimica et Cosmochimica Acta, v. 67, p. 171-183.

Möller, P., Morteani, G., Dulski, P., and Preinfalk, C., 2009, Vapour/liquid fractionation of rare earths, Y^{3+}, Na^{+}, K^{+}, NH_4^{+}, Cl^{-}, HCO_3^{-}, SO_4^{2-} and borate in fluids from the Piancastagnaio geothermal field, Italy: Geothermics, v. 38, p. 360-369.

Monecke, T., Kempe, U., Monecke, J., Sala, M., and Wolf, D., 2002, Tetrad effect in rare earth element distribution patterns: a method of quantification with application to rock and mineral samples from granite-related rare metal deposits: Geochimica et Cosmochimica Acta, v. 66, p. 1185-1196.

Monecke, T., Kempe, U., Trinkler, M., Thomas, R., Dulski, P., and Wagner, T., 2011, Unusual rare earth element fractionation in a tin-bearing magmatic-hydrothermal system: Geology, v. 39, p. 295–298.

Moscati, R.J., and Neymark, L.A., 2020, U-Pb geochronology of tin deposits associated with the Cornubian Batholith of southwest England: Direct dating of cassiterite by in situ LA-ICPMS: Mineralium Deposita, v. 55, p. 1-20.

Neymark, L.A., Holm-Denoma, C.S., and Moscati, R.J., 2018, In situ LA-ICPMS U–Pb dating of cassiterite without a known-age matrix-matched reference material: Examples from worldwide tin deposits spanning the Proterozoic to the Tertiary: Chemical Geology, v. 483, p. 410-425.

Palma, V.V., 1981, The San Rafael tin-copper deposit, SE Peru: Unpublished M.Sc. thesis, Queen’s University, Kingston, Ontario, 235 p.

Parsons, I., 1978, Feldspars and fluids in cooling plutons: Mineralogical Magazine, v. 42, p. 1-17.

Parsons, I., Rex, D.C., Guise, P., and Halliday, A.N., 1988, Argon-loss by alkali feldspars: Geochimica et Cosmochimica Acta, v. 52, p. 1097-1112.

Parsons, I., Brown, W.L., and Smith, J.V., 1999, $^{40}Ar/^{39}Ar$ thermochronology using alkali feldspars: real thermal history or mathematical mirage of microtexture?: Contributions to Mineralogy and Petrology, v. 136, p. 92-110.

Paton, C., Hellstrom, J., Paul, B., Woodhead, J., and Hergt, J., 2011, Iolite: Freeware for the visualisation and processing of mass spectrometric data: Journal of Analytical Atomic Spectrometry, v. 26, p. 2508-2518.

Pettke, T., Oberli, F., Audétat, A., Guillong, M., Simon, A.C., Hanley, J.J., and Klemm, L.M., 2012, Recent developments in element concentration and isotope ratio analysis of individual fluid inclusions by laser ablation single and multiple collector ICP-MS: Ore Geology Reviews, v. 44, p. 10-38.

Pirrie, D., Butcher, A.R., Power, M.R., Gottlieb, P., and Miller, G.L., 2004, Rapid quantitative mineral and phase analysis using automated scanning electron microscopy (QemSCAN): Potential applications in forensic geoscience: Geological Society of London Special Publication, v. 232, p. 123-136.

Plimer, I.R., Lu, J., and Kleeman, J.D., 1991, Trace and rare earth elements in cassiterite—sources of components for the tin deposits of the Mole Granite, Australia: Mineralium Deposita, v. 26, p. 267-274.

Plümper, O., and Putnis, A., 2009, The complex hydrothermal history of granitic rocks: multiple feldspar replacement reactions under subsolidus conditions: Journal of Petrology, v. 50, p. 967-987.

Prado Flores, E., 2015, San Rafael Tin Mine, Peru: Geology, mineralogy, O and H stable isotopes, and fluid inclusions microthermometry of the deep level 3600m: Unpublished M.Sc. thesis, University of Geneva, Switzerland, 89 p.

Putnis, A., 2002, Mineral replacement reactions: from macroscopic observations to microscopic mechanisms: Mineralogical Magazine, v. 66, p. 689-708.

1297 Putnis, A., 2009, Mineral replacement reactions. In Thermodynamics and Kinetics of Water-
1298 Rock Reaction (E.H. Oelkers and J. Schott, Eds): Reviews in Mineralogy and
1299 Geochemistry, v. 70, p. 87-124.
1300 Quang, C.X., Clark, A.H., W. Lee, J.K., and Hawkes, N., 2005, Response of supergene
1301 processes to episodic Cenozoic uplift, pediment erosion, and ignimbrite eruption in the
1302 porphyry copper province of southern Peru: Economic Geology, v. 100, p. 87-114.
1303 Rice, C.M., Steele, G.B., Barfod, D.N., Boyce, A.J., and Pringle, M.S., 2005, Duration of
1304 magmatic, hydrothermal, and supergene activity at Cerro Rico de Potosi, Bolivia:
1305 Economic Geology, v. 100, p. 1647-1656.
1306 Roberts, H.J., Kelley, S.P., and Dahl, P.S., 2001, Obtaining geologically meaningful ^{40}Ar–^{39}Ar
1307 ages from altered biotite: Chemical Geology, v. 172, p. 277-290.
1308 Rottier, B., Kouzmanov, K., Ovtcharova, M., Ulianov, A., Wälle, M., Selby, D., and Fontboté,
1309 L., 2020, Multiple rejuvenation episodes of a silicic magma reservoir at the origin of the
1310 large diatreme-dome complex and porphyry-type mineralization events at Cerro de Pasco
1311 (Peru): Lithos, v. 376, p. 105766.
1312 Rudnick, R.L., and Gao, S., 2014, Composition of the continental crust: Treatise on
1313 Geochemistry (Second Edition), v. 4, p. 1-51.
1314 Sandeman, H.A., Clark, A.H., and Farrar, E., 1995, An integrated tectono-magmatic model for
1315 the evolution of the southern Peruvian Andes (13–20°S) since 55 Ma: International
1316 Geology Reviews, v. 37, p. 1039–1073.
1317 Sandeman, H.A., Clark, A.H., Farrar, E., and Pauca, G.A., 1997, Lithostratigraphy, petrology
1318 and ^{40}Ar-^{39}Ar geochronology of the Crucero Supergroup, Puno department, SE Peru:
1319 Journal of South American Earth Sciences, v. 10, p. 223-245.
1320 Schaen, A.J., Jicha, B.R., Hodges, K.V., Vermeesch, P., Stelten, M.E., Mercer, C.M., Phillips,
1321 D., Rivera, T.A., Jourdan, F., Matchan, E.L., Hemming, S.R., Morgan, L.E., Kelley, S.P.,

Cassata, W.S., Heizler, M.T., Vasconcelos, P.M., Benowitz, J.A., Koppers, A.A.P., Mark, D.F., Niespolo, E.M., Sprain, C.J., Hames, W.E., Kuiper, K.F., Turrin, B.D., Renne, P.R., Ross, J., Nomade, S., Guillou, H., Webb, L.E., Cohen, B.A., Calvert, A.T., Joyce, N., Ganerød, M., Wijbrans, J., Ishizuka, O., He, H., Ramirez, A., Pfänder, J.A., Lopez-Martínez, M., Qiu, H., and Singer, B.S., 2021, Interpreting and reporting $^{40}Ar/^{39}Ar$ geochronologic data: GSA Bulletin, v. 133, p. 461-487.

Schirra, M., and Laurent, O., 2021, Petrochronology of hydrothermal rutile in mineralized porphyry Cu systems: Chemical Geology, v. 581, p. 120407.

Shannon, R.D., 1976, Revised effective ionic radii and systematic studies of interatomic distances in halides and chalcogenides: Acta Crystallographica, v. 32, p. 751–767.

Shmulovich, K., Heinrich, W., Möller, P., and Dulski, P., 2002, Experimental determination of REE fractionation between liquid and vapour in the systems NaCl–H_2O and $CaCl_2$–H_2O up to 450°C: Contributions to Mineralogy and Petrology, v. 144, p. 257-273.

Spell, T.L., and McDougall, I., 2003, Characterization and calibration of $^{40}Ar/^{39}Ar$ dating standards: Chemical Geology, v. 198, p. 189-211.

Spencer, E.T., Wilkinson, J.J., Creaser, R.A., and Seguel, J., 2015, The distribution and timing of molybdenite mineralization at the El Teniente Cu-Mo porphyry deposit, Chile: Economic Geology, v. 110, p. 387-421.

Steiger, R.H., and Jäger, E., 1977, Subcommission on geochronology: convention on the use of decay constants in geo- and cosmochronology: Earth and Planetary Science Letters, v. 36, p. 359-362.

Tang, Y., Cui, K., Zheng, Z., Gao, J., Han, J., Yang, J., and Liu, L., 2020, LA-ICP-MS U-Pb geochronology of wolframite by combining NIST series and common lead-bearing MTM as the primary reference material: implications for metallogenesis of South China: Gondwana Research, v. 83, p. 217–231.

1347 Tapster, S., and Bright, J.W.G., 2020, High-precision ID-TIMS Cassiterite U-Pb systematics
1348 using a low-contamination hydrothermal decomposition: implications for LA-ICP-MS and
1349 ore deposit geochronology: Geochronology, v. 2, p. 425-441.
1350 Tapster, S., Condon, D.J., Naden, J., Noble, S.R., Petterson, M.G., Roberts, N.M.W., Saunders,
1351 A.D., and Smith, D.J., 2016, Rapid thermal rejuvenation of high-crystallinity magma
1352 linked to porphyry copper deposit formation; evidence from the Koloula Porphyry
1353 Prospect, Solomon Islands: Earth and Planetary Science Letters, v. 442, p. 206-217.
1354 Taylor, R.G, 1979, Geology of Tin Deposits: Developments in Economic Geology, v. 11, 543
1355 p.
1356 Tindle, A.G., and Breaks, F.W., 1998, Oxide minerals of the Separation Rapids rare-element
1357 granitic pegmatite group, northwestern Ontario: The Canadian Mineralogist, v. 36, p. 609-
1358 635.
1359 Turneaure, F.S., 1971, The Bolivian tin-silver province: Economic Geology, v. 66, p. 215-225.
1360 Vermeesch, P., 2018, IsoplotR: A free and open toolbox for geochronology: Geoscience
1361 Frontiers, v. 9, p. 1479-1493.
1362 Villa, I.M., De Bièvre, P., Holden, N.E., and Renne, P.R., 2015, IUPAC-IUGS recommendation
1363 on the half-life of ^{87}Rb: Geochimica et Cosmochimica Acta, v. 164, p. 382-385.
1364 Villagómez, D., and Spikings, R., 2013, Thermochronology and tectonics of the Central and
1365 Western Cordilleras of Colombia: Early Cretaceous–Tertiary evolution of the northern
1366 Andes: Lithos, v. 160, p. 228-249.
1367 von Quadt, A., Erni, M., Martinek, K., Moll, M., Peytcheva, I., and Heinrich, C.A., 2011, Zircon
1368 crystallization and the lifetimes of ore-forming magmatic-hydrothermal systems: Geology,
1369 v. 39, p. 731-734.

Wagner, T., Mlynarczyk, M.S., Williams-Jones, A.E., and Boyce, A.J., 2009, Stable isotope constraints on ore formation at the San Rafael tin-copper deposit, Southeast Peru: Economic Geology, v. 104, p. 223-248.

Wright, T.L., 1968, X-ray and optical study of alkali feldspar—II. An X-ray method for determining the composition and structural state from measurement of 2θ values for three reflections: American Mineralogist, v. 53, p. 88–104.

Xiong, Y.Q., Shao, Y.J., Zhou, H.D., Wu, Q.H., Liu, J.P., Wei, H.T., Zhao, R.C., and Cao, J.Y., 2017, Ore-forming mechanism of quartz-vein-type W-Sn deposits of the Xitian district in SE China: Implications from the trace element analysis of wolframite and investigation of fluid inclusions: Ore Geology Reviews, v. 83, p. 152-173.

Zhang, D.L., Peng, J.T., Hu, R.Z., Yuan, S.D., and Zheng, D.S., 2011, The closure of U–Pb isotope system in cassiterite and its reliability for dating: Geological Review, v. 57, p. 549–554 (in Chinese with English abstract).

Zhang, R., Lehmann, B., Seltmann, R., Sun, W., and Li, C., 2017, Cassiterite U-Pb geochronology constrains magmatic-hydrothermal evolution in complex evolved granite systems: The classic Erzgebirge tin province (Saxony and Bohemia): Geology, v. 45, p. 1095-1098.

Zhang, Q., Zhang, R.Q., Gao, J.F., Lu, J.J., and Wu, J.W., 2018, In-situ LA-ICP-MS trace element analyses of scheelite and wolframite: Constraints on the genesis of veinlet-disseminated and vein-type tungsten deposits, South China: Ore Geology Reviews, v. 99, p. 166-179.

Figure captions

Fig. 1. Geological map and cross-section of San Rafael district, southeast Peru. (A) Location of the San Rafael Sn (-Cu) deposit in the Central Andean tin belt (modified from Mlynarczyk et al., 2003). (B) Geological map of San Rafael district compiled from new mapping and integrating older data (modified from Harlaux et al., 2020). The background corresponds to a digital elevation model of the San Rafael area. (C) Longitudinal cross-section of the San Rafael lode system (modified from Harlaux et al., 2020). Map line of section X-X′ is shown on (B). Abbreviations: QG = Quenamari granite, RD = ring dikes, SRG = San Rafael granite, TL = tourmaline-bearing leucogranite.

Fig. 2. Photographs of representative samples from San Rafael showing the different stages of the paragenetic sequence. (A) Main cordierite-biotite megacrystic granite containing centimetric K-feldspar phenocrysts showing weak hydrothermal alteration (sample SRG-38, San Rafael mine, level 3,610 masl). (B) Quartz-muscovite greisen containing dumortierite and tourmaline (stage I) located in the upper part of the San Rafael granite (sample SRG-133B, San Rafael surface, elevation 4,926 masl). (C) Pre-ore quartz-tourmaline vein (stage I) crosscutting the cordierite-biotite megacrystic granite and surrounded by an alteration halo of albite (sample PSR-47, San Rafael mine, level 3,610 masl). (D) Botryoidal cassiterite ("wood tin") intergrown with chlorite and quartz (stage II) in a bonanza ore from the San Rafael lode (sample SR-16-KK-14, San Rafael mine, level 4,440 masl). (E) Coarse-grained cassiterite in a quartz-chlorite vein/breccia body (stage II) from the Kimberly vein (sample SRG-95, San Rafael mine, level 3,950 masl). (F) Quartz-adularia-fluorite assemblage (stage IV) overgrown on a quartz-chlorite-chalcopyrite vein (stage III) crosscutting an altered metasedimentary rock at Quenamari (sample SRG-43, Quenamari surface, elevation 4,920 masl). Abbreviations: Ab = albite, Adl =

adularia, Bt = biotite, Ccp = chalcopyrite, Chl = chlorite, Cst = cassiterite, Dum = dumortierite, Fl = fluorite, Kfs = K-feldspar, Ms = muscovite, Pl = plagioclase, Qtz = quartz, Tur = tourmaline.

Fig. 3. Transmitted light photomicrographs (TL) and QEMSCAN false-color images of representative samples from San Rafael illustrating the different stages of the paragenetic sequence. (A) Weakly altered K-feldspar megacrystic cordierite-biotite granite (sample SRG-38, San Rafael mine, level 3,610 masl). (B) Quartz-muscovite greisen containing dumortierite and tourmaline (stage I) in the upper part of the San Rafael granite (sample SRG-133B, San Rafael surface, elevation 4,926 masl). (C) Quartz-tourmaline vein (stage I) cutting the cordierite-biotite megacrystic granite and surrounded by albitic alteration halo (sample SRG-68, San Rafael mine, level 4,310 masl). (D) Botryoidal cassiterite ("wood tin") intergrown with chlorite (stage II) in a quartz-chlorite vein/breccia from the San Rafael lode (sample SR-16-KK-14, San Rafael mine, level 4,440 masl). (E) Coarse-grained cassiterite in a quartz-chlorite breccia (stage II) from the Kimberly vein (sample SRG-95, San Rafael mine, level 3,950 masl). (F) Quartz-adularia-fluorite assemblage (stage IV) overgrown on a quartz-chlorite-sulfide-adularia±cassiterite vein (stage III) crosscutting an altered metasedimentary rock (sample SRG-43, Quenamari surface, elevation 4,920 masl). Abbreviations: Ab = albite, Adl = adularia, Ap = apatite, Bt = biotite, Ccp = chalcopyrite, Chl = chlorite, Cst = cassiterite, Dum = dumortierite, Fl = fluorite, Kfs = K-feldspar, Ms = muscovite, Pl = plagioclase, Py = pyrite, Qtz = quartz, Tur = tourmaline. The white color corresponds to pixels non-attributed to a mineral phase (mostly vugs).

Fig. 4. Revised paragenetic sequence of the San Rafael deposit incorporating previous descriptions (Palma, 1981; Kontak and Clark, 2002; Mlynarczyk et al., 2003; Mlynarczyk and

Williams-Jones, 2006; Wagner et al., 2009; Corthay, 2014; Prado Flores, 2015; Gialli et al., 2019; Harlaux et al., 2020, 2021b) and new observations presented in this study from San Rafael and Quenamari. Thick and thin lines correspond to relative mineral abundance.

Fig. 5. Summary of X-ray diffraction data for K-feldspars from the San Rafael and Quenamari granites plotted in the polymorph diagram of Wright (1968) that summarizes the different states of Si-Al ordering. The data plotted are from Kontak (1985) and details are provided therein and in Kontak et al. (1984). The samples selected for dating are indicated by numbers, all of which have COCA prefix. Note the following: 1) glassy samples from the same age and petrologically similar Antauta granitic dike (see text for discussion) are disordered and equate to sanidine structurally; 2) samples from the granitic rocks (i.e., ring dikes) at Quenamari have more disordered structures than the main granite; 3) metasomatic samples are more orthoclase-enriched compared to the fresh samples, in particular for the San Rafael intrusion; and 4) for some samples, the least altered and their metasomatic equivalents are plotted.

Fig. 6. $^{40}Ar/^{39}Ar$ age spectra for biotite from the San Rafael megacrystic cordierite-biotite granite showing plateau ages. The reported degree of alteration of the host rock and K contents of biotite are from Kontak and Clark (2002). All ages are reported at 2σ level of confidence.

Fig. 7. $^{40}Ar/^{39}Ar$ age spectra for biotite from the San Rafael megacrystic cordierite-biotite granite showing disturbed patterns. The reported degree of alteration of the host rock and K contents of biotite are from Kontak and Clark (2002). All ages are reported at 2σ level of confidence.

Fig. 8. $^{40}Ar/^{39}Ar$ age spectra for K-feldspar phenocrysts from the San Rafael megacrystic cordierite-biotite granite showing U-shaped pattern and pseudo-plateau ages. The reported degree of alteration of the host rock and orthoclase molar contents (mol.% Or) are from Kontak and Clark (2002). All ages are reported at 2σ level of confidence.

Fig. 9. $^{40}Ar/^{39}Ar$ age spectra for muscovite from the San Rafael deposit yielding plateau ages. The reported degree of alteration of the host rock and K contents of muscovite are from Palma (1981) and Kontak (1985). All ages are reported at 2σ level of confidence.

Fig. 10. $^{40}Ar/^{39}Ar$ age spectra for adularia from the San Rafael deposit yielding plateau ages. The reported degree of alteration of the host rock and K contents of adularia are from Palma (1981) and this work. All ages are reported at 2σ level of confidence.

Fig. 11. Tera-Wasserburg U-Pb Concordia diagrams for cassiterite from the San Rafael deposit. Data-point error ellipses are 2σ.

Fig. 12. Variation diagrams of selected trace elements in cassiterite from the San Rafael deposit. Linear regressions through data points are shown for botryoidal cassiterite (dashed line) and coarse-grained cassiterite (solid line).

Fig. 13. (A) Trace element contents of cassiterite from the San Rafael deposit normalized to upper continental crust values (UCC from Rudnick and Gao, 2014). (B) Rare earth element contents of cassiterite from the San Rafael deposit normalized to C1 chondrite values (McDonough and Sun, 1995). The grey field correspond to the range of concentrations for

cassiterite from Oligocene-Miocene Sn deposits in the Bolivian tin belt (Gemmrich et al., 2021).

Fig. 14. (A) Transmitted-light (TL) photomicrograph and (B) cathodoluminescence (CL) optical image of botryoidal cassiterite (sample SRG-62-1, San Rafael vein, level 4,310 masl) from the San Rafael deposit with locations of laser ablation spots (white circles). (C) Trace element composition along a profile (analyses 1–21) perpendicular to growth banding.

Fig. 15. (A) Transmitted-light (TL) photomicrograph and (B) cathodoluminescence (CL) optical image of coarse-grained cassiterite (sample SRG-95, Kimberly vein, level 3,950 masl) from the San Rafael deposit with locations of laser ablation spots (white circles). (C) Trace element composition along a profile (analyses 1–23) perpendicular to growth banding.

Fig. 16. Summary of geochronological data for the San Rafael Sn (-Cu) deposit. Uncertainties are reported at 2σ level of confidence. Data sources include this study and previous work of (1) Kontak and Clark (2002), (2) Harlaux et al. (2021b), (3) Kontak et al. (1987), (4) Clark et al. (1983), and (5) Kontak et al. (1986).

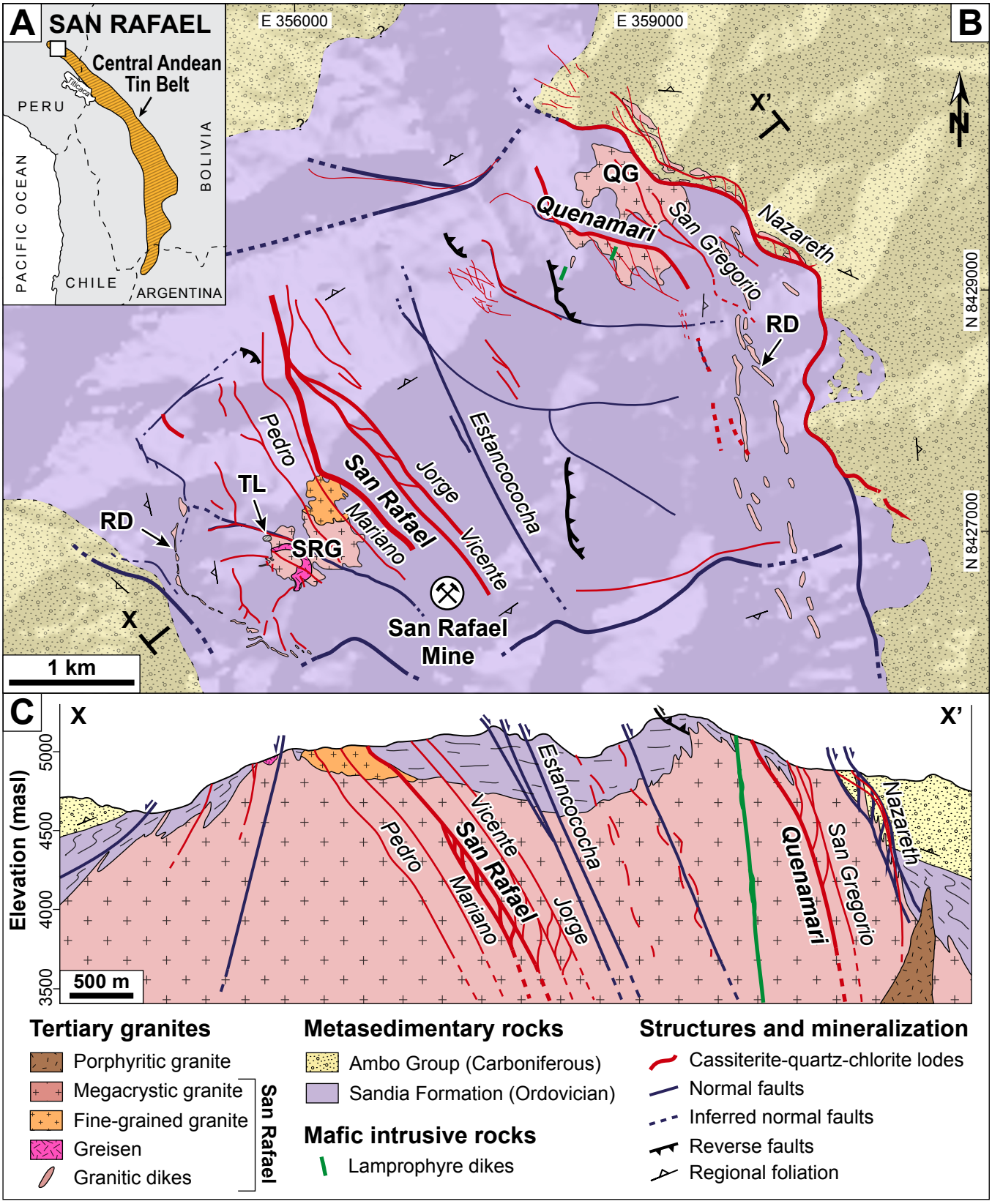
A
SAN RAFAEL
Central Andean
Tin Belt
PERU
BOLIVIA
PACIFIC OCEAN
CHILE
ARGENTINA
B
E 356000
E 359000
N 8429000
N 8427000
X'
N
QG
Quenamari
San Gregorio
Nazareth
RD
Pedro
San Rafael
Jorge
Estancococha
Mariano
Vicente
TL
SRG
RD
X
San Rafael
Mine
1 km
C
X
X'
Elevation (masl)
5000
4500
4000
3500
500 m
Pedro
Vicente
San Rafael
Mariano
Jorge
Estancococha
Quenamari
San Gregorio
Nazareth
Tertiary granites
Porphyritic granite
Megacrystic granite
Fine-grained granite
Greisen
Granitic dikes
San Rafael
Metasedimentary rocks
Ambo Group (Carboniferous)
Sandia Formation (Ordovician)
Mafic intrusive rocks
Lamprophyre dikes
Structures and mineralization
Cassiterite-quartz-chlorite lodes
Normal faults
Inferred normal faults
Reverse faults
Regional foliation

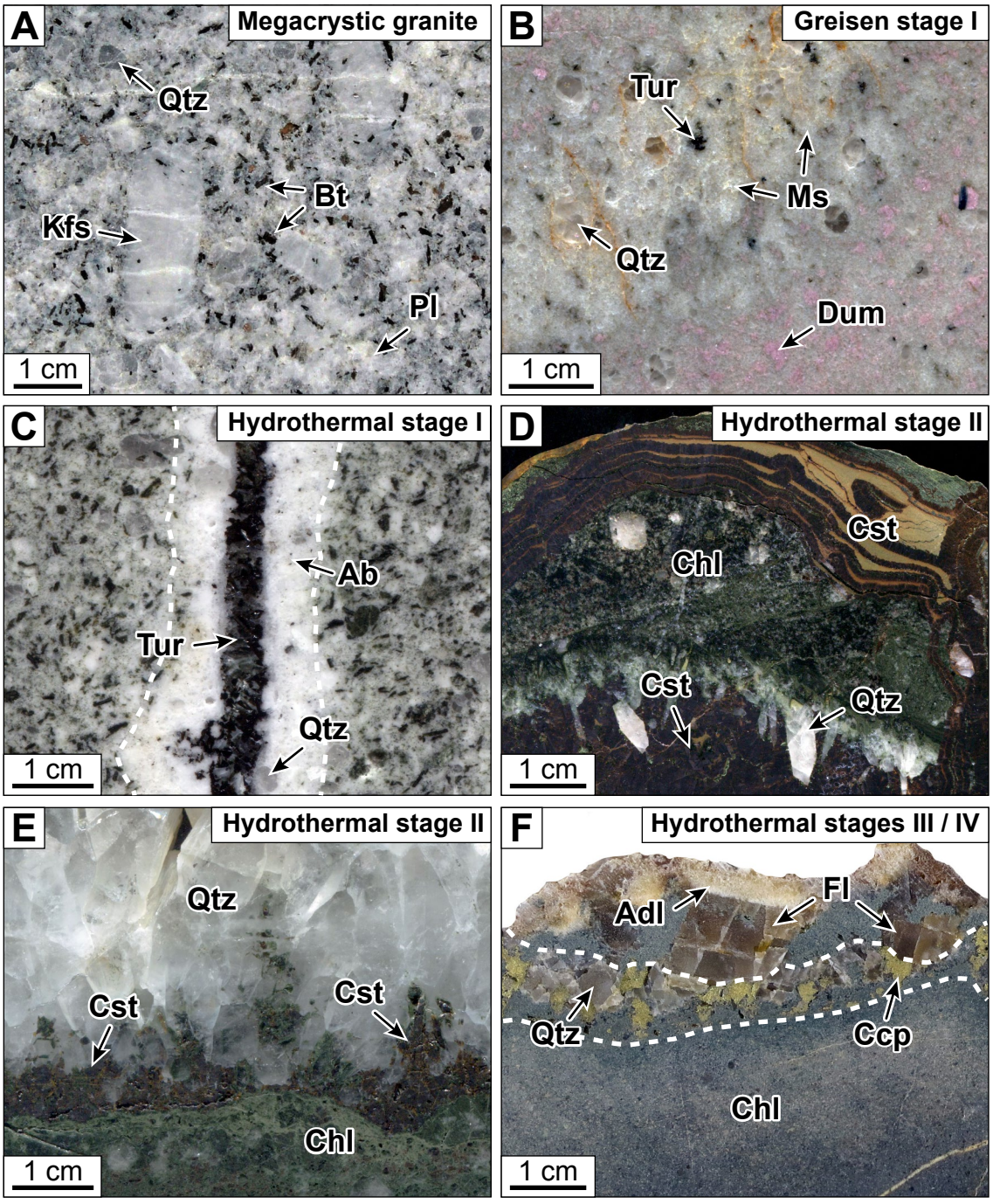
A
Megacrystic granite
Qtz
Bt
Kfs
Pl
1 cm
B
Greisen stage I
Tur
Ms
Qtz
Dum
1 cm
C
Hydrothermal stage I
Ab
Tur
Qtz
1 cm
D
Hydrothermal stage II
Cst
Chl
Cst
Qtz
1 cm
E
Hydrothermal stage II
Qtz
Cst
Cst
Chl
1 cm
F
Hydrothermal stages III / IV
Adl
Fl
Qtz
Ccp
Chl
1 cm

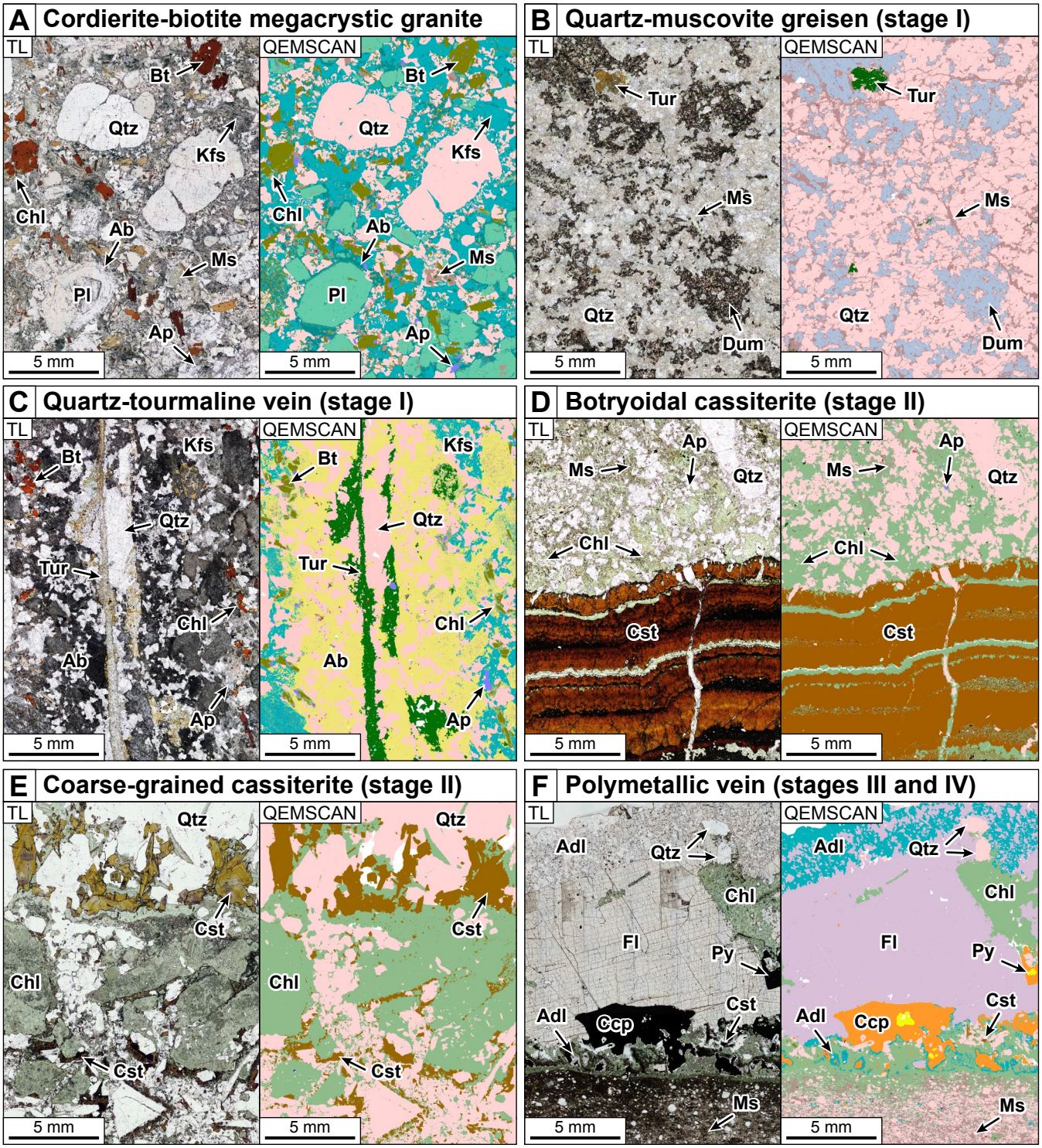
A Cordierite-biotite megacrystic granite
TL
QEMSCAN
Bt
Qtz
Kfs
Chl
Ab
Ms
Pl
Ap
5 mm
B Quartz-muscovite greisen (stage I)
Tur
Ms
Qtz
Dum
C Quartz-tourmaline vein (stage I)
Tur
D Botryoidal cassiterite (stage II)
Cst
E Coarse-grained cassiterite (stage II)
F Polymetallic vein (stages III and IV)
Adl
Fl
Py
Ccp

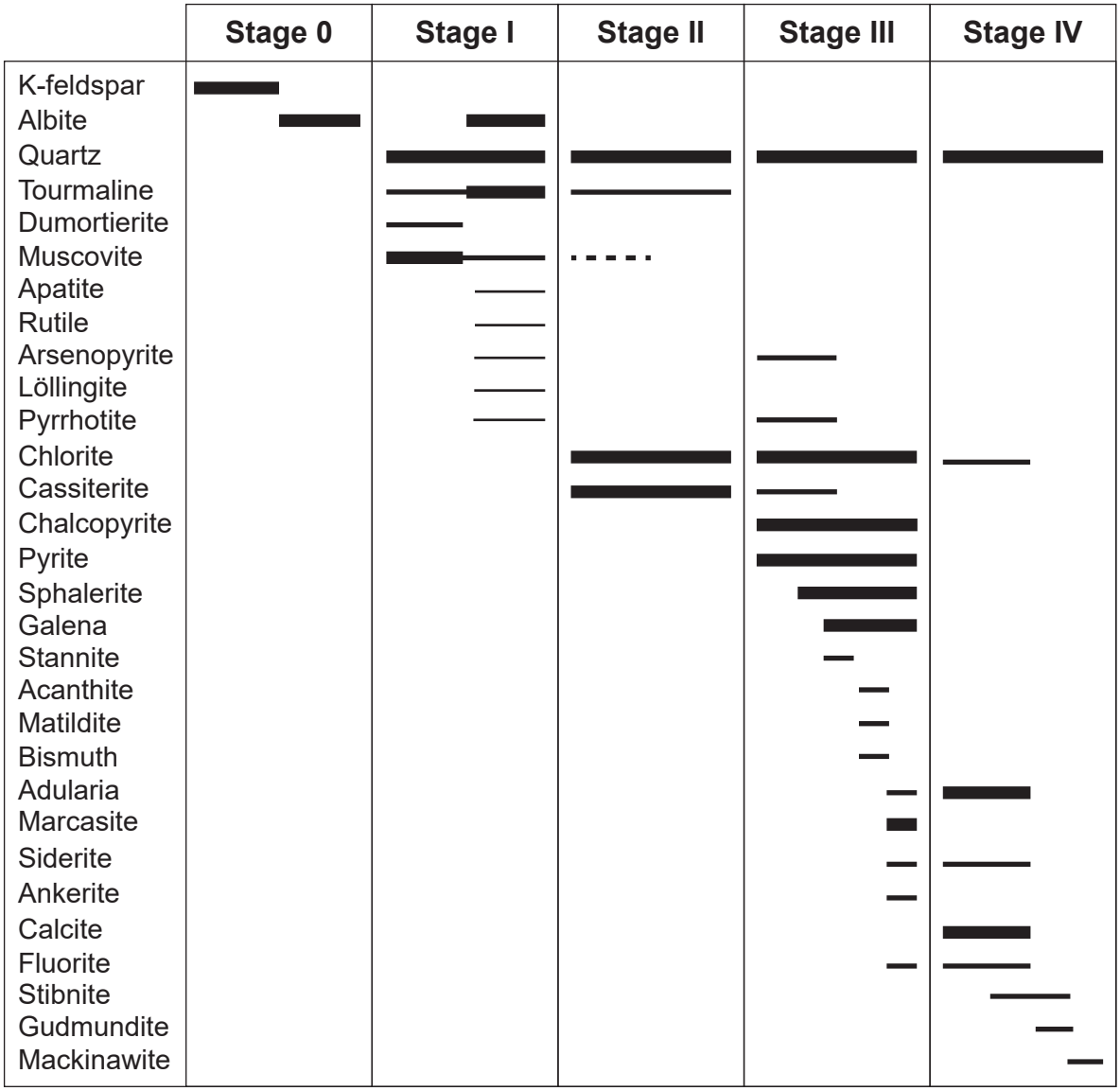
Stage 0
Stage I
Stage II
Stage III
Stage IV
K-feldspar
Albite
Quartz
Tourmaline
Dumortierite
Muscovite
Apatite
Rutile
Arsenopyrite
Löllingite
Pyrrhotite
Chlorite
Cassiterite
Chalcopyrite
Pyrite
Sphalerite
Galena
Stannite
Acanthite
Matildite
Bismuth
Adularia
Marcasite
Siderite
Ankerite
Calcite
Fluorite
Stibnite
Gudmundite
Mackinawite

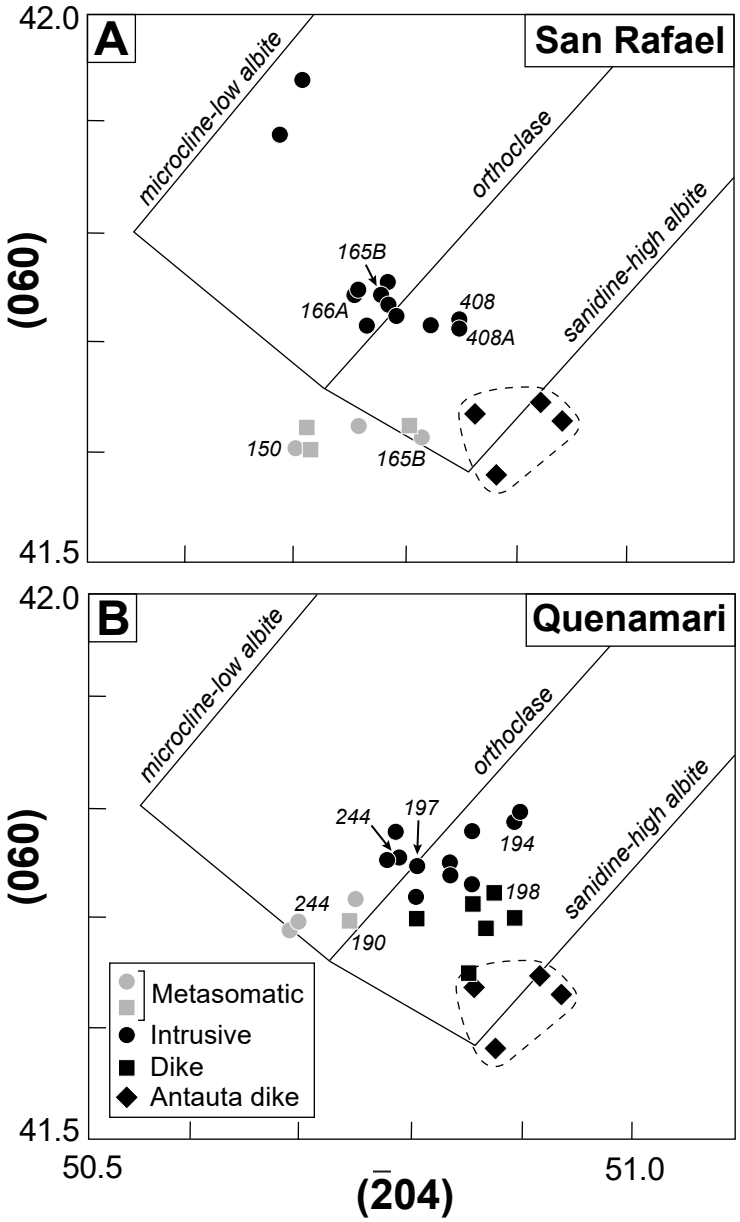
A
San Rafael
microcline-low albite
orthoclase
sanidine-high albite
165B
166A
408
408A
150
165B
42.0
41.5
(060)
B
Quenamari
microcline-low albite
orthoclase
sanidine-high albite
244
197
194
198
244
190
Metasomatic
Intrusive
Dike
Antauta dike
42.0
41.5
50.5
51.0
(2̄04)

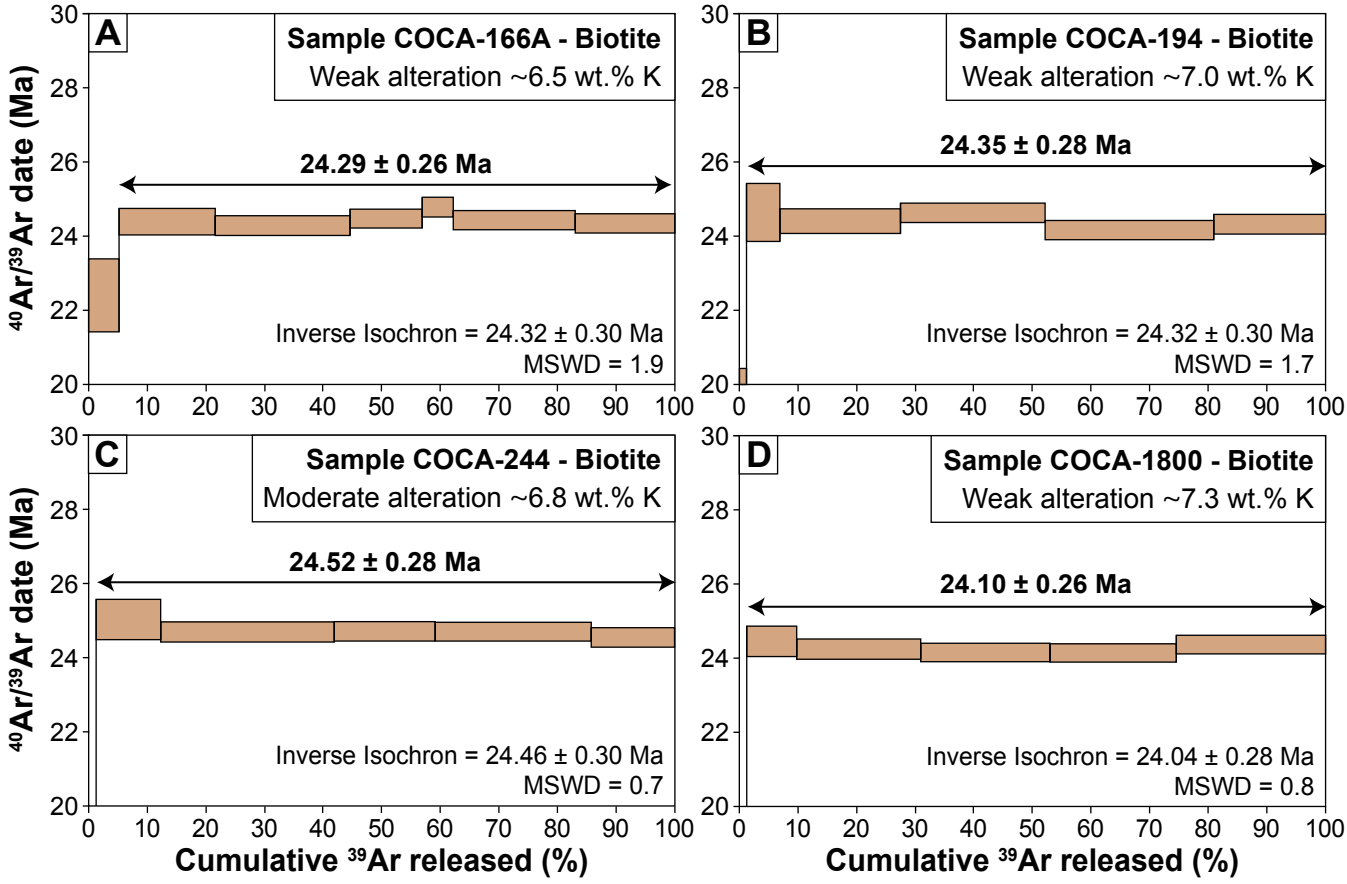
A
Sample COCA-166A - Biotite
Weak alteration ~6.5 wt.% K
24.29 ± 0.26 Ma
Inverse Isochron = 24.32 ± 0.30 Ma
MSWD = 1.9
B
Sample COCA-194 - Biotite
Weak alteration ~7.0 wt.% K
24.35 ± 0.28 Ma
Inverse Isochron = 24.32 ± 0.30 Ma
MSWD = 1.7
C
Sample COCA-244 - Biotite
Moderate alteration ~6.8 wt.% K
24.52 ± 0.28 Ma
Inverse Isochron = 24.46 ± 0.30 Ma
MSWD = 0.7
D
Sample COCA-1800 - Biotite
Weak alteration ~7.3 wt.% K
24.10 ± 0.26 Ma
Inverse Isochron = 24.04 ± 0.28 Ma
MSWD = 0.8
40Ar/39Ar date (Ma)
Cumulative 39Ar released (%)

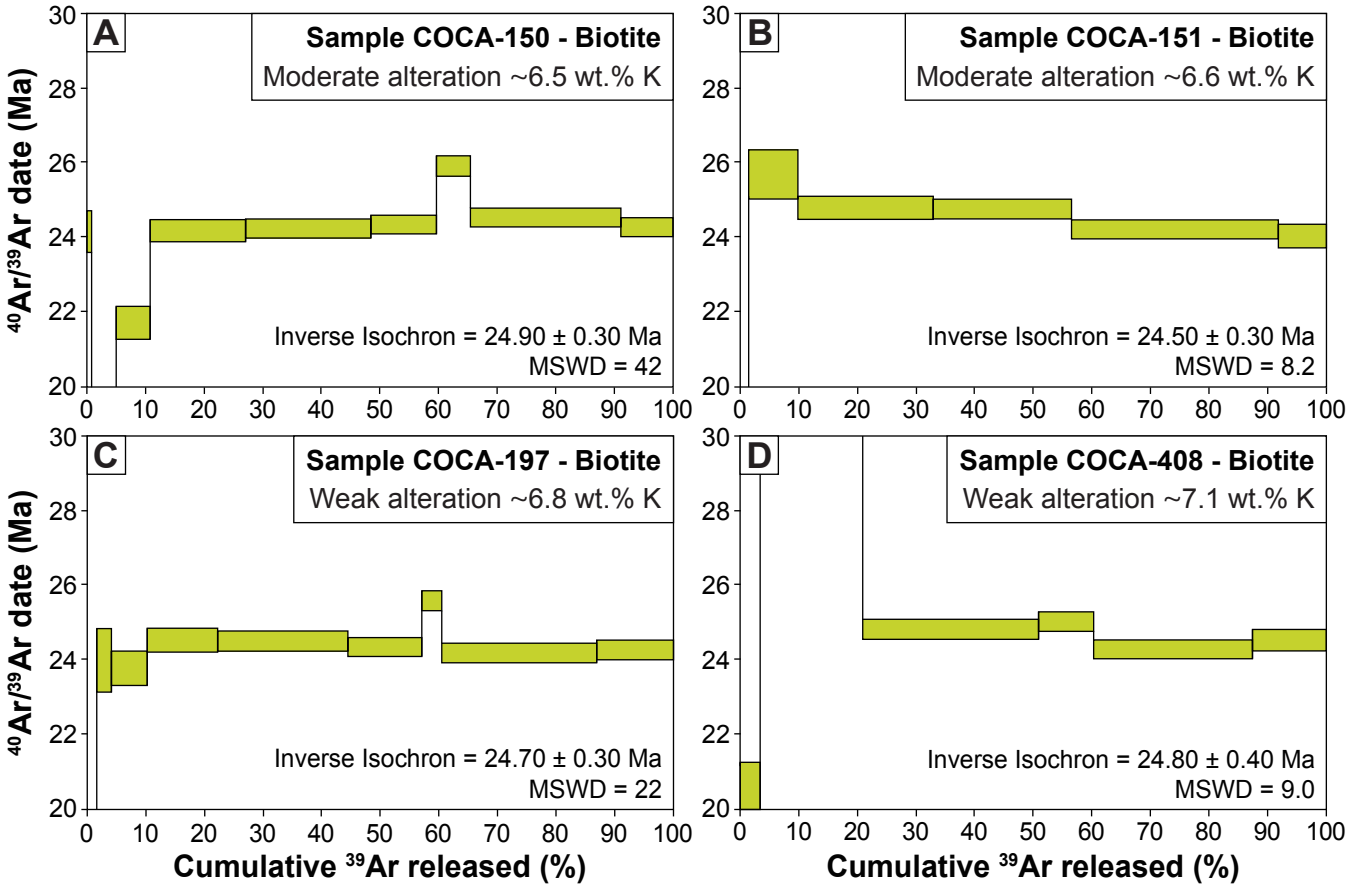
A
Sample COCA-150 - Biotite
Moderate alteration ~6.5 wt.% K
Inverse Isochron = 24.90 ± 0.30 Ma
MSWD = 42
B
Sample COCA-151 - Biotite
Moderate alteration ~6.6 wt.% K
Inverse Isochron = 24.50 ± 0.30 Ma
MSWD = 8.2
C
Sample COCA-197 - Biotite
Weak alteration ~6.8 wt.% K
Inverse Isochron = 24.70 ± 0.30 Ma
MSWD = 22
D
Sample COCA-408 - Biotite
Weak alteration ~7.1 wt.% K
Inverse Isochron = 24.80 ± 0.40 Ma
MSWD = 9.0
40Ar/39Ar date (Ma)
Cumulative 39Ar released (%)

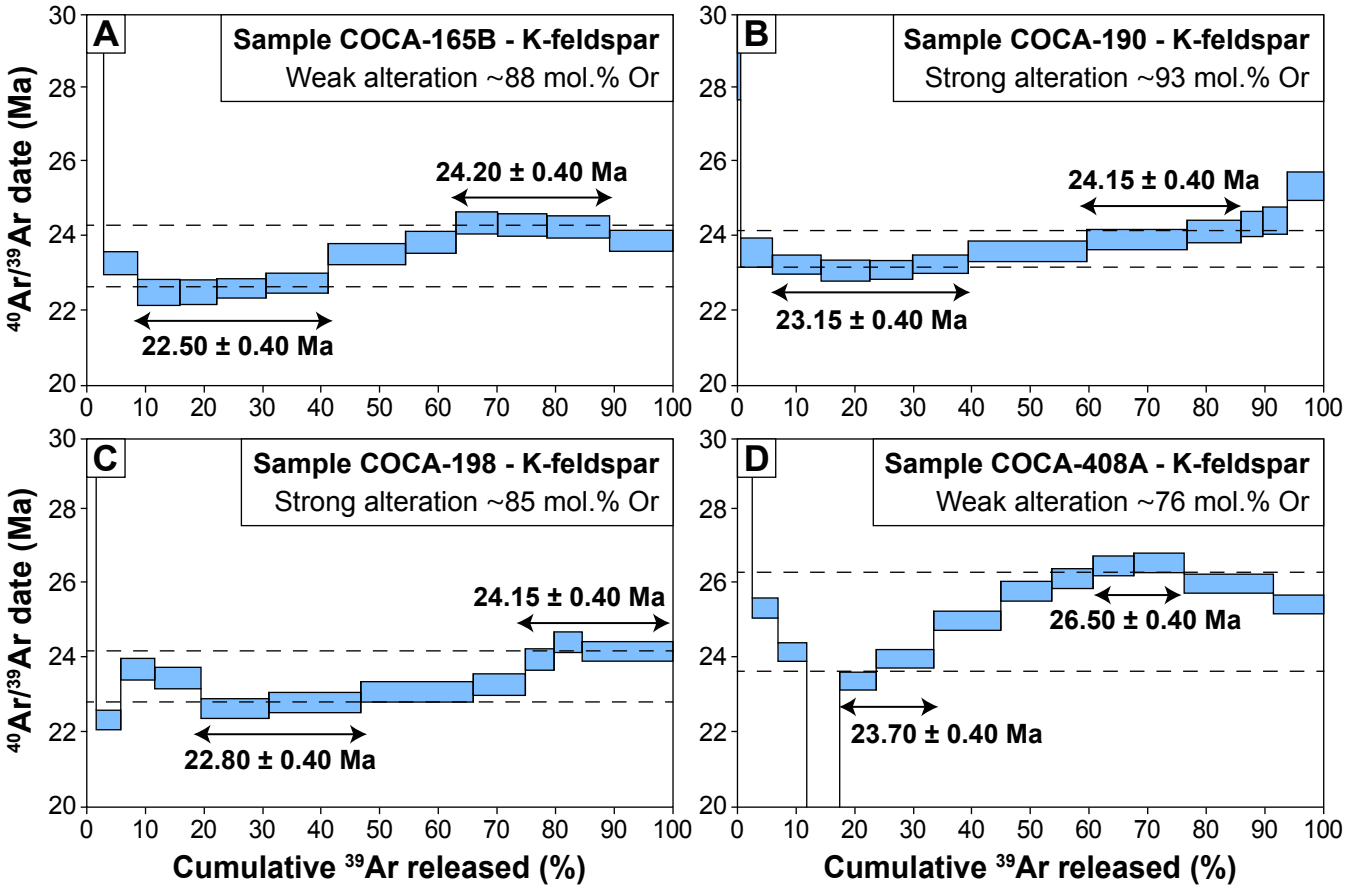
A
Sample COCA-165B - K-feldspar
Weak alteration ~88 mol.% Or
24.20 ± 0.40 Ma
22.50 ± 0.40 Ma
B
Sample COCA-190 - K-feldspar
Strong alteration ~93 mol.% Or
24.15 ± 0.40 Ma
23.15 ± 0.40 Ma
C
Sample COCA-198 - K-feldspar
Strong alteration ~85 mol.% Or
24.15 ± 0.40 Ma
22.80 ± 0.40 Ma
D
Sample COCA-408A - K-feldspar
Weak alteration ~76 mol.% Or
26.50 ± 0.40 Ma
23.70 ± 0.40 Ma
40Ar/39Ar date (Ma)
Cumulative 39Ar released (%)

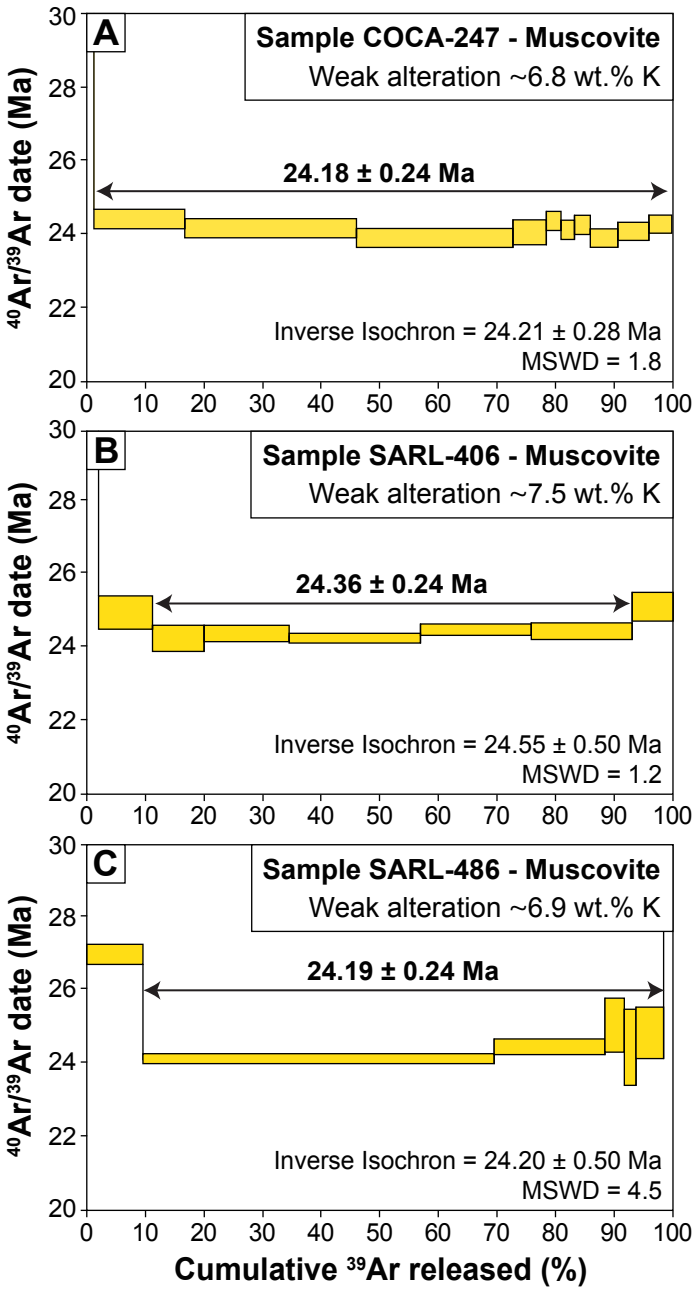
A
Sample COCA-247 - Muscovite
Weak alteration ~6.8 wt.% K
24.18 ± 0.24 Ma
Inverse Isochron = 24.21 ± 0.28 Ma
MSWD = 1.8
B
Sample SARL-406 - Muscovite
Weak alteration ~7.5 wt.% K
24.36 ± 0.24 Ma
Inverse Isochron = 24.55 ± 0.50 Ma
MSWD = 1.2
C
Sample SARL-486 - Muscovite
Weak alteration ~6.9 wt.% K
24.19 ± 0.24 Ma
Inverse Isochron = 24.20 ± 0.50 Ma
MSWD = 4.5
40Ar/39Ar date (Ma)
Cumulative 39Ar released (%)
20
22
24
26
28
30
0
10
20
30
40
50
60
70
80
90
100

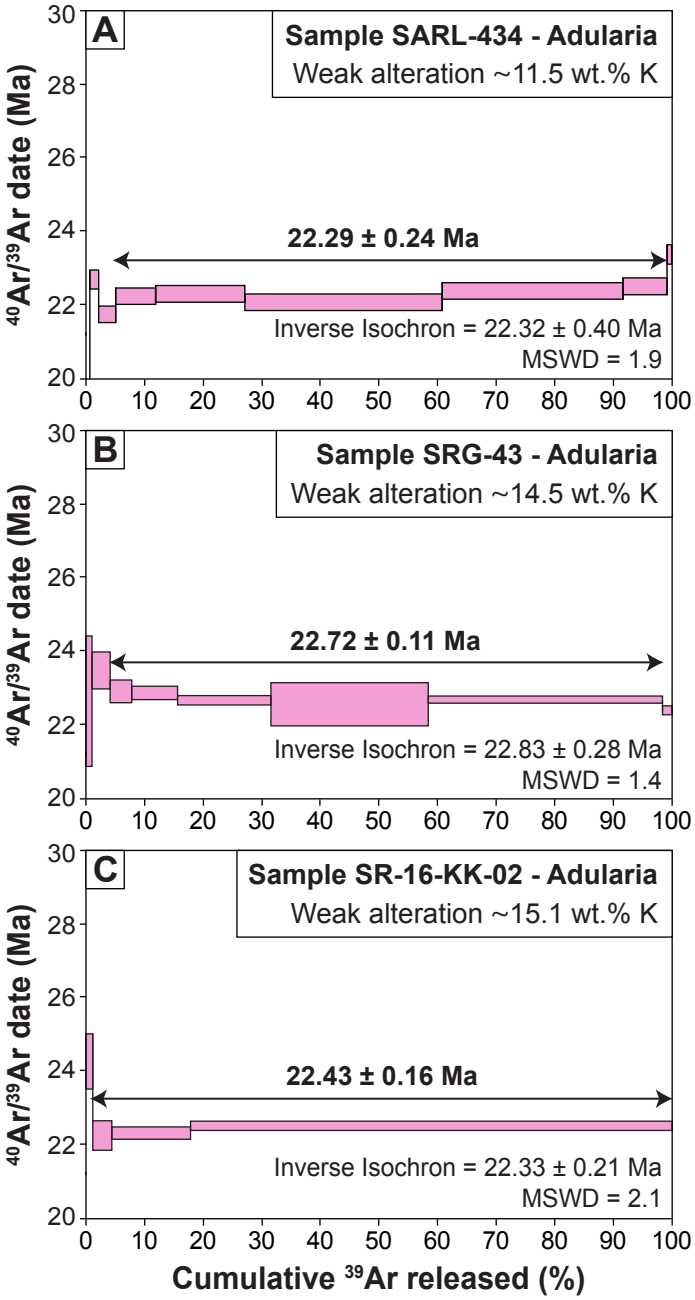
A
Sample SARL-434 - Adularia
Weak alteration ~11.5 wt.% K
22.29 ± 0.24 Ma
Inverse Isochron = 22.32 ± 0.40 Ma
MSWD = 1.9
B
Sample SRG-43 - Adularia
Weak alteration ~14.5 wt.% K
22.72 ± 0.11 Ma
Inverse Isochron = 22.83 ± 0.28 Ma
MSWD = 1.4
C
Sample SR-16-KK-02 - Adularia
Weak alteration ~15.1 wt.% K
22.43 ± 0.16 Ma
Inverse Isochron = 22.33 ± 0.21 Ma
MSWD = 2.1
40Ar/39Ar date (Ma)
Cumulative 39Ar released (%)
20
22
24
26
28
30
0
10
20
30
40
50
60
70
80
90
100

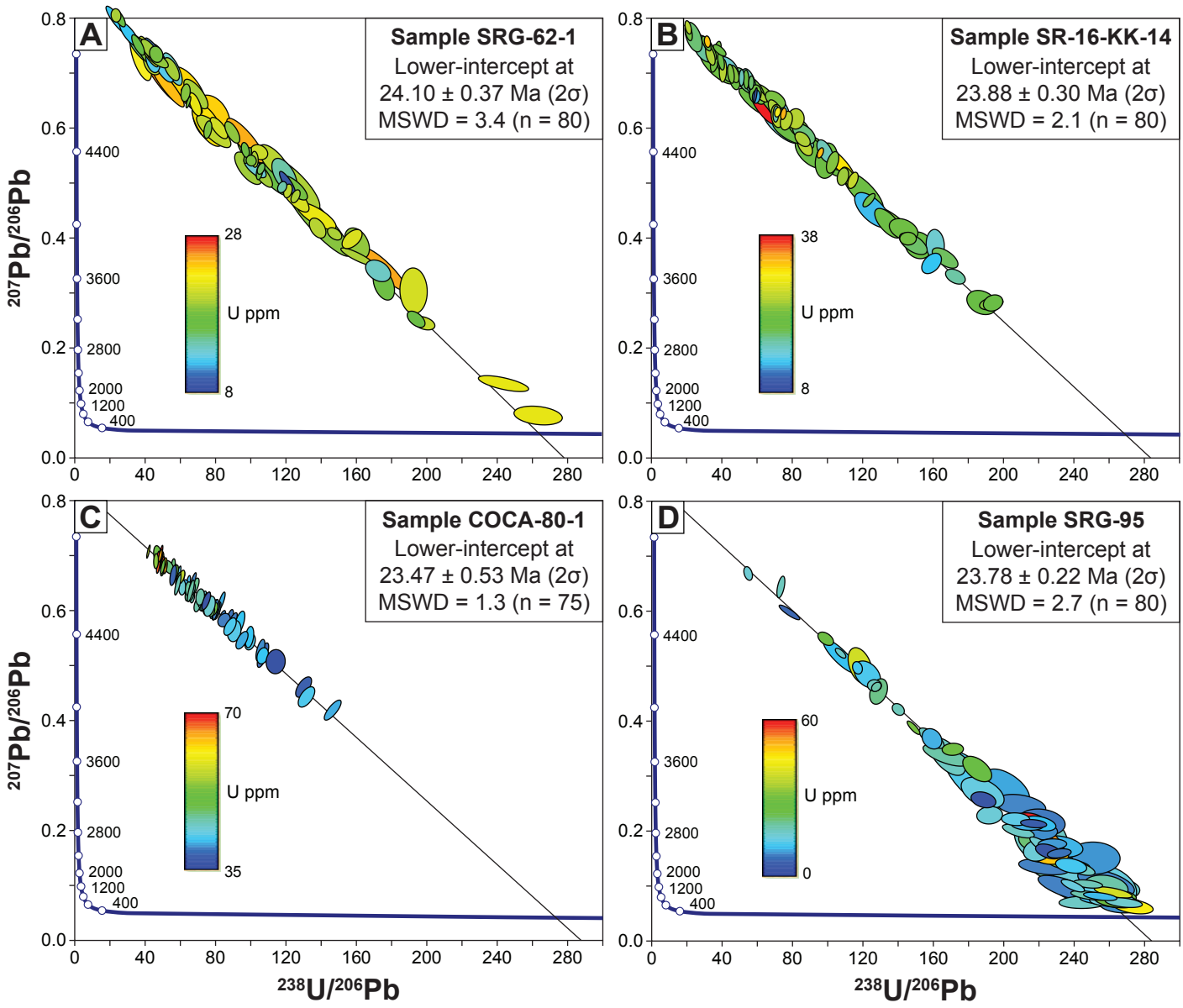
A
Sample SRG-62-1
Lower-intercept at
24.10 ± 0.37 Ma (2σ)
MSWD = 3.4 (n = 80)
B
Sample SR-16-KK-14
Lower-intercept at
23.88 ± 0.30 Ma (2σ)
MSWD = 2.1 (n = 80)
C
Sample COCA-80-1
Lower-intercept at
23.47 ± 0.53 Ma (2σ)
MSWD = 1.3 (n = 75)
D
Sample SRG-95
Lower-intercept at
23.78 ± 0.22 Ma (2σ)
MSWD = 2.7 (n = 80)
U ppm
28
8
38
70
35
60
0
4400
3600
2800
2000
1200
400
0.0
0.2
0.4
0.6
0.8
0
40
80
120
160
200
240
280
207Pb/206Pb
238U/206Pb

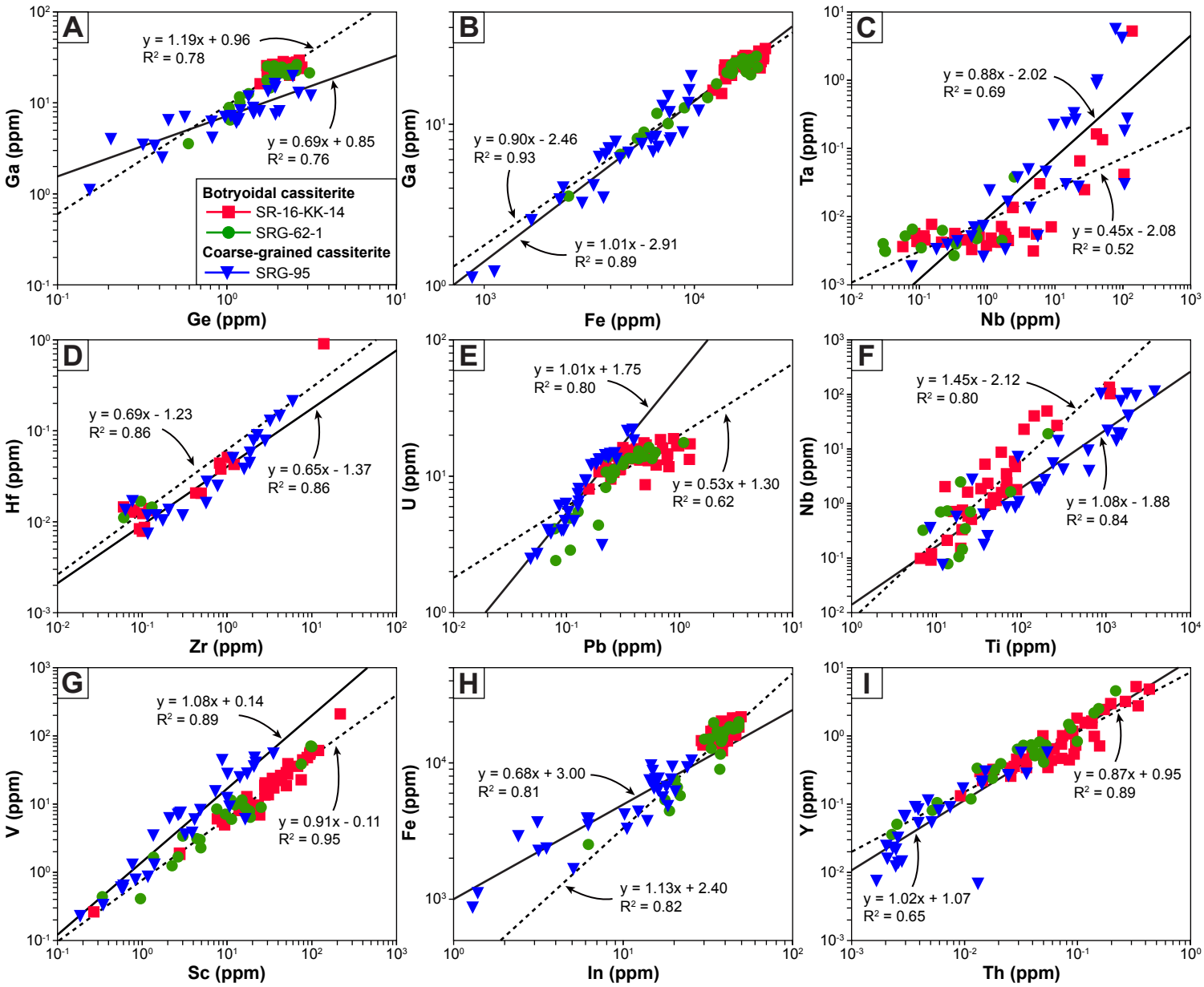
A
y = 1.19x + 0.96
R² = 0.78
y = 0.69x + 0.85
R² = 0.76
Botryoidal cassiterite
SR-16-KK-14
SRG-62-1
Coarse-grained cassiterite
SRG-95
Ga (ppm)
Ge (ppm)
B
y = 0.90x - 2.46
R² = 0.93
y = 1.01x - 2.91
R² = 0.89
Ga (ppm)
Fe (ppm)
C
y = 0.88x - 2.02
R² = 0.69
y = 0.45x - 2.08
R² = 0.52
Ta (ppm)
Nb (ppm)
D
y = 0.69x - 1.23
R² = 0.86
y = 0.65x - 1.37
R² = 0.86
Hf (ppm)
Zr (ppm)
E
y = 1.01x + 1.75
R² = 0.80
y = 0.53x + 1.30
R² = 0.62
U (ppm)
Pb (ppm)
F
y = 1.45x - 2.12
R² = 0.80
y = 1.08x - 1.88
R² = 0.84
Nb (ppm)
Ti (ppm)
G
y = 1.08x + 0.14
R² = 0.89
y = 0.91x - 0.11
R² = 0.95
V (ppm)
Sc (ppm)
H
y = 0.68x + 3.00
R² = 0.81
y = 1.13x + 2.40
R² = 0.82
Fe (ppm)
In (ppm)
I
y = 0.87x + 0.95
R² = 0.89
y = 1.02x + 1.07
R² = 0.65
Y (ppm)
Th (ppm)

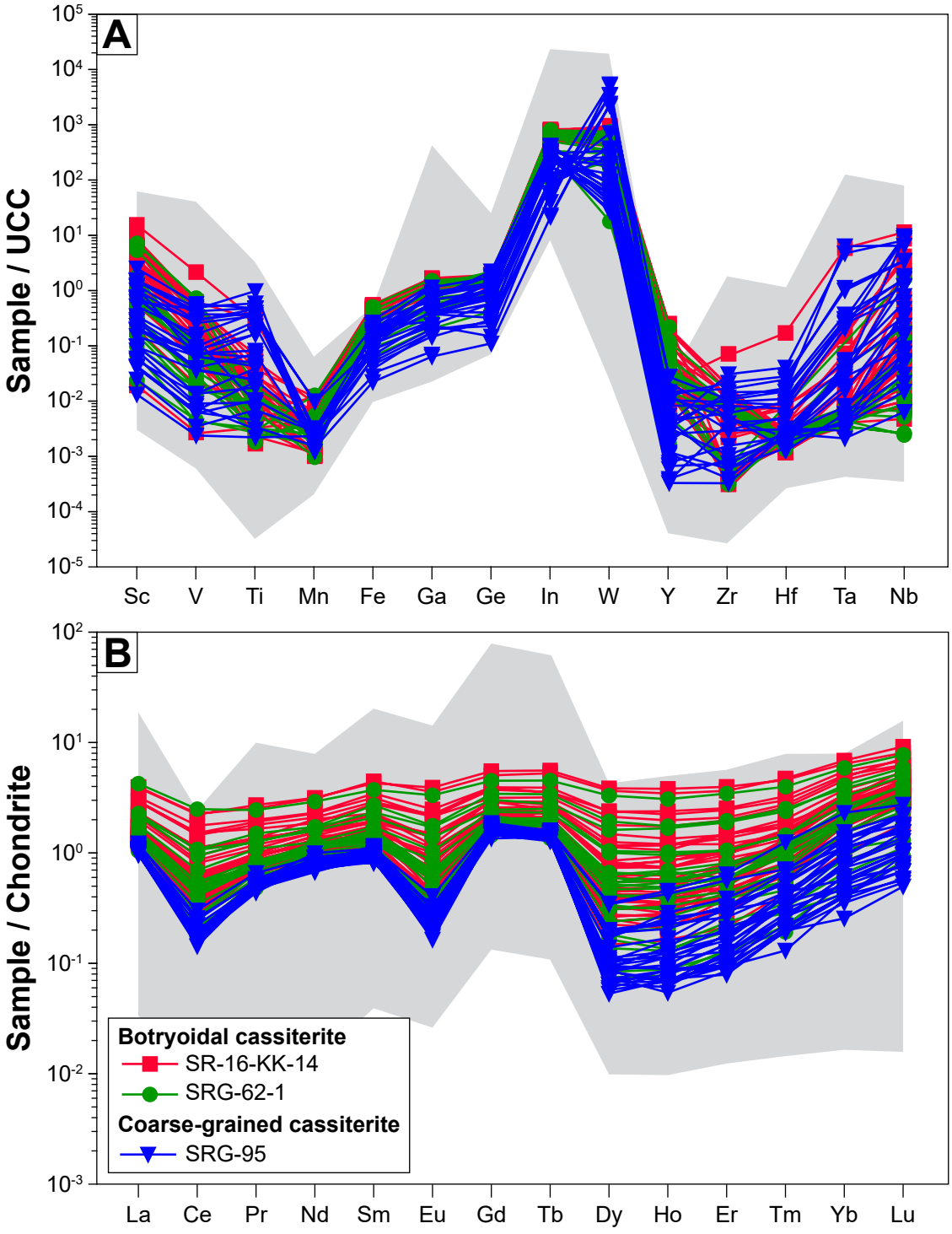
A
Sample / UCC
10^5
10^4
10^3
10^2
10^1
10^0
10^{-1}
10^{-2}
10^{-3}
10^{-4}
10^{-5}
Sc V Ti Mn Fe Ga Ge In W Y Zr Hf Ta Nb
B
Sample / Chondrite
10^2
10^1
10^0
10^{-1}
10^{-2}
10^{-3}
Botryoidal cassiterite
SR-16-KK-14
SRG-62-1
Coarse-grained cassiterite
SRG-95
La Ce Pr Nd Sm Eu Gd Tb Dy Ho Er Tm Yb Lu

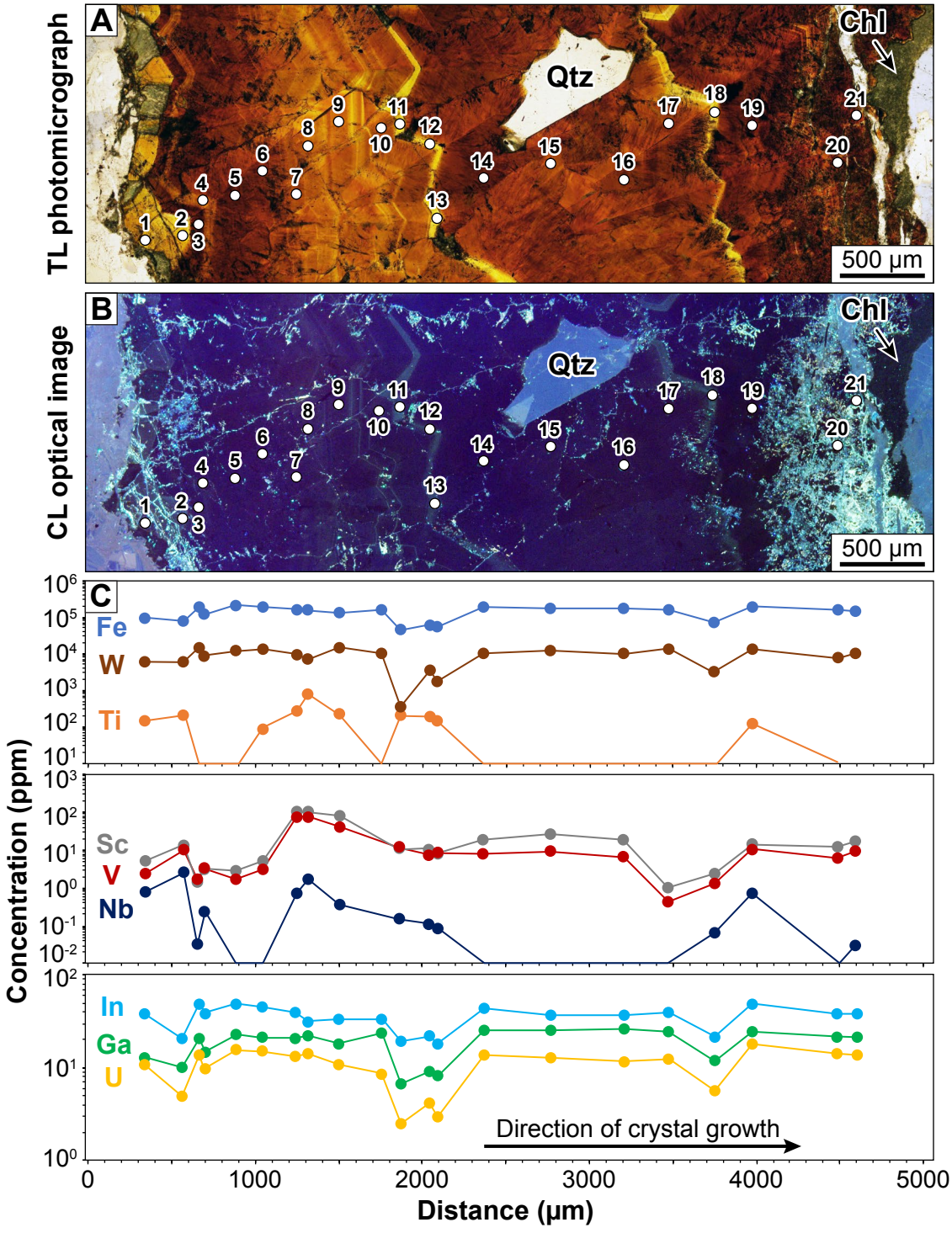
A
TL photomicrograph
Qtz
Chl
500 μm
B
CL optical image
Qtz
Chl
500 μm
C
Fe
W
Ti
Sc
V
Nb
In
Ga
U
Concentration (ppm)
Direction of crystal growth
Distance (μm)

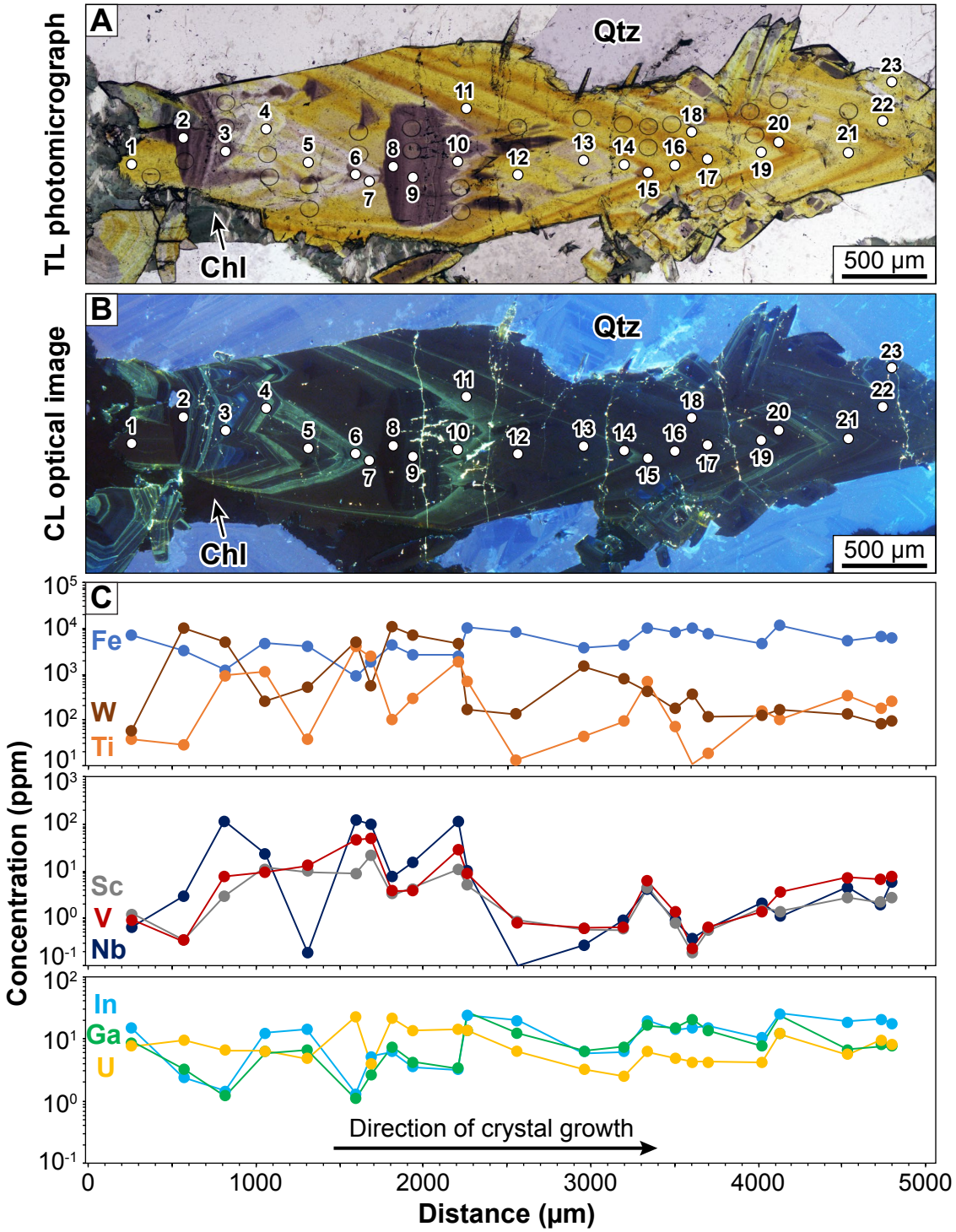
A
TL photomicrograph
Qtz
Chl
500 µm
B
CL optical image
Qtz
Chl
500 µm
C
Fe
W
Ti
Sc
V
Nb
In
Ga
U
Concentration (ppm)
Direction of crystal growth
Distance (µm)
0
1000
2000
3000
4000
5000

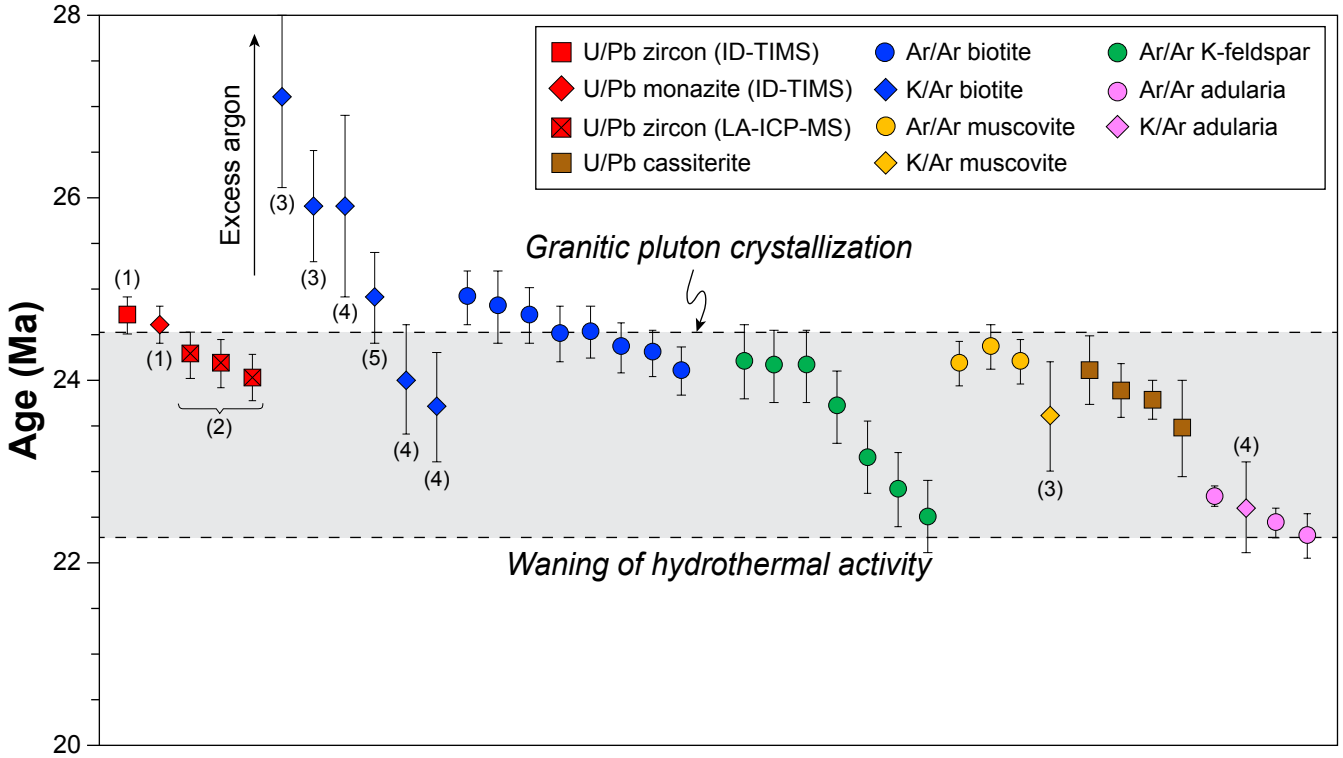
Age (Ma)
28
26
24
22
20
U/Pb zircon (ID-TIMS)
U/Pb monazite (ID-TIMS)
U/Pb zircon (LA-ICP-MS)
U/Pb cassiterite
Ar/Ar biotite
K/Ar biotite
Ar/Ar muscovite
K/Ar muscovite
Ar/Ar K-feldspar
Ar/Ar adularia
K/Ar adularia
Excess argon
Granitic pluton crystallization
Waning of hydrothermal activity
(1)
(1)
(2)
(3)
(3)
(4)
(5)
(4)
(4)
(3)
(4)

Table 1. Description, locality, and ages of the dated samples from the San Rafael deposit in this study.

Sample	Description	Paragenetic stage	Locality	Northing	Easting	Age (Ma)	Method
			Biotite				
COCA-150	Cordierite-biotite megacrystic granite	Magmatic stage	San Rafael mine, level 4,533 masl	8427012	356711	24.9 ± 0.30	$^{40}Ar/^{39}Ar$ step-heating
COCA-151	Cordierite-biotite megacrystic granite	Magmatic stage	San Rafael mine, level 4,533 masl	8427012	356711	24.50 ± 0.30	$^{40}Ar/^{39}Ar$ step-heating
COCA-166A	Cordierite-biotite megacrystic granite	Magmatic stage	San Rafael surface, elevation 4,830 masl	8426735	356623	24.29 ± 0.26 ^{P}	$^{40}Ar/^{39}Ar$ step-heating
COCA-194	Cordierite-biotite megacrystic granite	Magmatic stage	Quenamari surface, elevation 4,955 masl	8429472	359020	24.35 ± 0.28 ^{P}	$^{40}Ar/^{39}Ar$ step-heating
COCA-197	Cordierite-biotite megacrystic granite	Magmatic stage	Quenamari surface, elevation 5,020 masl	8429045	359053	24.70 ± 0.30	$^{40}Ar/^{39}Ar$ step-heating
COCA-244	Cordierite-biotite megacrystic granite	Magmatic stage	Quenamari surface, elevation 4,885 masl	8429596	359263	24.52 ± 0.28 ^{P}	$^{40}Ar/^{39}Ar$ step-heating
COCA-408	Cordierite-biotite megacrystic granite	Magmatic stage	San Rafael mine, level 4,533 masl	8426669	356408	24.80 ± 0.40	$^{40}Ar/^{39}Ar$ step-heating
COCA-1800	Cordierite-biotite megacrystic granite	Magmatic stage	San Rafael mine, level 4,200 masl	-	-	24.10 ± 0.26 ^{P}	$^{40}Ar/^{39}Ar$ step-heating
			K-feldspar				
COCA-165B	Cordierite-biotite megacrystic granite	Magmatic stage	San Rafael mine, level 4,533 masl	8426735	356623	22.50 ± 0.40	$^{40}Ar/^{39}Ar$ step-heating
COCA-190	Porphyry ring dike east of the Quenamari granite	Magmatic stage	Quenamari surface, elevation 4,845 masl	8428279	359875	23.15 ± 0.40	$^{40}Ar/^{39}Ar$ step-heating
COCA-198	Porphyry ring dike east of the Quenamari granite	Magmatic stage	Quenamari surface, elevation 4,800 masl	8428975	359747	22.80 ± 0.40	$^{40}Ar/^{39}Ar$ step-heating
COCA-408A	Cordierite-biotite megacrystic granite	Magmatic stage	San Rafael mine, level 4,533 masl	8426669	356408	23.70 ± 0.40	$^{40}Ar/^{39}Ar$ step-heating
			Muscovite				
COCA-247	Muscovite in greisenized megacrystic granite	Stage I	San Rafael surface, elevation 4,970 masl	8426827	356089	24.18 ± 0.24 ^{P}	$^{40}Ar/^{39}Ar$ step-heating
SARL-406	Muscovite in greisenized megacrystic granite	Stage I	San Rafael mine, San Rafael vein, level 4,770 masl	-	-	24.36 ± 0.24 ^{P}	$^{40}Ar/^{39}Ar$ step-heating
SARL-486	Muscovite in greisenized metasedimentary rocks	Stage I	San Rafael mine, level 4,820 masl	-	-	24.19 ± 0.24 ^{P}	$^{40}Ar/^{39}Ar$ step-heating
			Cassiterite				
SRG-62-1	Botryoidal cassiterite in quartz-chlorite vein	Stage II	San Rafael mine, San Rafael vein, level 4,310 masl	8428686	356568	24.10 ± 0.37	U-Pb LA-ICP-MS
SR-16-KK-14	Botryoidal cassiterite in quartz-chlorite breccia	Stage II	San Rafael mine, San Rafael vein, level 4,400 masl	8427179	356753	23.88 ± 0.30	U-Pb LA-ICP-MS
COCA-80-1	Botryoidal cassiterite in quartz-chlorite vein	Stage II	San Rafael mine, San Rafael vein, level 4,533 masl	8427179	356753	23.47 ± 0.53	U-Pb LA-ICP-MS
SRG-95	Coarse-grained cassiterite in quartz-chlorite vein	Stage II	San Rafael mine, Kimberly vein, level 3,950 masl	8428283	356745	23.78 ± 0.22	U-Pb LA-ICP-MS
			Adularia				
SARL-434	Quartz-adularia vein in megacrystic granite	Stage III	San Rafael mine, Jorge vein, level 4,820 masl	8427237	357218	22.29 ± 0.24 ^{P}	$^{40}Ar/^{39}Ar$ step-heating
SRG-43	Quartz-fluorite-adularia vein in shale	Stage IV	Quenamari surface, Alejandrina vein, elevation 4,920 masl	8429278	359323	22.72 ± 0.11 ^{P}	$^{40}Ar/^{39}Ar$ step-heating
SR-16-KK-02	Quartz-adularia veinlets in shale	Stage IV	Estancococha area, elevation 4,720 masl	8426862	357575	22.43 ± 0.16 ^{P}	$^{40}Ar/^{39}Ar$ step-heating

UTM coordinates are given in the 19L zone. All age uncertainties are reported at 2σ. P = plateau age.